

**Historical and projected trends in extreme heat events in
Minnesota urban areas**

A THESIS
SUBMITTED TO THE FACULTY OF THE
UNIVERSITY OF MINNESOTA
BY

Jonathan Francis Halsted Birkel

IN PARTIAL FULFILLMENT OF THE REQUIREMENTS
FOR THE DEGREE OF
MASTER OF SCIENCE

Dr. Tracy Twine

October 2021

© Jonathan Francis Halsted Birkel 2021

Acknowledgements

I would first like to thank my advisor, Dr. Tracy Twine, for her support and guidance throughout all stages of my graduate school experience both on and off campus, and her encouragement to explore a wide variety of directions in my research. I also thank Dr. Peter Snyder and Dr. Kathy Klink for their insights and feedback as members of my thesis committee.

I would like to acknowledge Dr. Stefan Liess for his WRF downscaling work that provided an important basis for this research, and for his technical support and guidance on working with climate model output data. I also would like to thank Dr. Scott Sheridan for running his SSC algorithms on the WRF outputs. I appreciate his patience with the volume of data I sent him and willingness to experiment with various approaches.

Additionally, I would like to express my gratitude toward Dr. Larry Kalkstein, Elizabeth Berg, and the Wisconsin Heat Health Network for the opportunity to work with them in exploring connections between heat and health outcomes. This project explicitly addressed topics more implicit in my thesis, and the steps we took and findings we reached had a large influence on the directions I ended up taking here.

I would like to thank all the faculty, staff, and students in the Land and Atmospheric Science program for fostering a welcoming and supportive environment, which was especially appreciated while we were unable to remain together on campus.

Finally, I would like to thank my partner, Erin, and everyone in both of our families. Being a graduate student and living through a global pandemic each brought plenty of challenges, and their love and support are what ultimately made getting through both at once possible.

Abstract

Extreme heat is often overlooked as a public health concern in Minnesota, where intraseasonal summer variability limits acclimatization to oppressive heat conditions. Specific categories of synoptic-scale air masses are linked to summer excess mortality and elevated health risk in the Midwestern United States, particularly within urban heat islands. Between 1948 and 2019, Minnesota's four largest urban areas have experienced narrowing diurnal temperature ranges and decreased nighttime cooling, while warmer and more humid air masses have increased in frequency at the expense of cooler and drier ones. Distinctions between urban and neighboring rural sites' diurnal temperature ranges across summer air masses are generally more significant in southern than northern Minnesota. This study utilized downscaled climate projections for mid and late 21st-century Minnesota, under RCP4.5 and RCP8.5 emissions scenarios, to generate daily spatial synoptic classifications, facilitating an evaluation of projected frequency and character trends in the highest-risk air masses. Most prominently, climate projections showed dramatic increases in both the frequency and temperature of days under the Dry Tropical air mass category, neither of which have changed significantly thus far across Minnesota's historical record. Frequency and duration of consecutive-day episodes of excess heat, as identified either by synoptic classifications or by the Excess Heat Factor, are likewise expected to increase more significantly in the future than they have in the past. Other projected trends, such as rising dew point temperatures and nighttime air temperatures, represent clearer continuations of historical trends. However, the magnitude, timing, and dependence on future carbon emissions of these trends are not

uniform across all air masses. With these results, the study aims to provide a basis for estimating future heat-related risks to human health.

List of Tables

Table 2.1: List of GCMs for boundary conditions, from Liess et al. (2021).	59
Table 3.1: Summary statistics for urban sites' air mass frequency (days per season), air temperature (T_a ; °C), and dew point temperature (T_d ; °C) trends over 1948-2019 within the May 20-September 10 season. Linear regression slopes are expressed as decadal rather than yearly changes. Bold slope and R^2 values indicate $p < 0.05$ significance. *Fargo's daily maximum DP temperatures increased with $p < 0.05$ significance, while DP temperatures at 15:00 did not. Conversely, Fargo's MT temperatures at 3:00 increased with $p < 0.05$ significance, while daily minimum MT temperatures did not. Statistical significance between daily and hourly datasets matched for all other trends.	60
Table 3.2: Summary statistics for paired urban and rural sites' trends in diurnal temperature range (°C) over 1948-2019 within the May 20-September 10 season. Linear regression slopes are expressed as decadal rather than yearly changes. Bold slope and R^2 values indicate $p < 0.05$ significance.	61
Table 3.3: Summary statistics for urban sites' trends in frequency (occurrences per summer) and duration (days per occurrence) of consecutive runs of 3 or more MT+/DT days over 1948-2019 within the May 20-September 10 season. Linear regression slopes are expressed as decadal rather than yearly changes. Bold slope and R^2 values indicate $p < 0.05$ significance.	62
Table 3.4: Summary statistics for urban sites' trends in positive-EHF heat wave events over 1948-2019. T_{95} indicates the 95th-percentile temperature threshold (°C), while EHF_{85} indicates the 85th-percentile EHF value threshold (°C ²). Frequency and duration are expressed as in Table 3.3. Heat wave season starting dates are expressed as Julian dates. Linear regression slopes are expressed as decadal rather than yearly changes. Bold slope and R^2 values indicate $p < 0.05$ significance. ..	63
Table 3.5: Allocation of daily SSC categories within all positive-EHF heat wave days and within severe heat wave days only. Values are expressed as total days over 1948-2019 and as percentages of each location's heat wave or severe heat wave days.	64

- Table 4.1:** Historical multi-model ensemble agreement with JJA monthly temperature averages (°C) and air mass frequency (days per May 20-September 10 season) in Minneapolis weather station observations. All rows represent 20 observations, with one value per year from 1980 to 1999, as shown in Figures 4.6-4.7. 65
- Table 4.2:** Summary statistics for simulated air mass frequency (days per season), as well as frequency (occurrences per season) and duration (days per occurrence) of consecutive runs of 3 or more MT+/DT days. All statistics represent Minneapolis within the May 20-September 10 season over four climate scenarios. Air mass frequencies and consecutive run frequencies represent 160 observations, with one value per model-year combination. Consecutive run durations represent individual events unaggregated by model or year (number of observations = $160 \times$ number of events per average model-year). Bold mean values indicate significant changes from HIST ($p < 0.05$ by t-test). 66
- Table 4.3:** Summary statistics for simulated Minneapolis air mass temperatures (°C) within May 20-September 10 over four climate scenarios. All rows summarize individual days unaggregated by model or year (number of observations = $160 \times$ days per average model-year). Bold mean values indicate significant changes from HIST ($p < 0.05$ by t-test). 67
- Table 4.4:** Summary statistics for simulated trends in positive-EHF heat wave events, defined either from each model's HIST T95 threshold and applied across all scenarios within that model ("no acclimatization"), or from each model-scenario combination's own T95 threshold ("full acclimatization"). All statistics represent Minneapolis within the May 20-September 10 season over four climate scenarios. T95 indicates the 95th-percentile temperature threshold (°C), while EHF85 indicates the 85th-percentile EHF value threshold (°C²); means and standard deviations for these summarize eight values, one from each model-scenario. Heat wave frequencies, heat wave season lengths, heat wave season starting dates (Julian date), number of heat wave days, and number of severe heat waves represent 160 observations, with one value per model-year combination. All other rows represent individual days or events unaggregated by model or year (number of observations = $160 \times$ number of days or events per average model-year). Bold mean values indicate significant changes from HIST ($p < 0.05$ by t-test). 68

List of Figures

Figure 2.1: Locations of weather stations from which historical temperature records were used. Larger markers labeled in bold represent urban airport stations.	69
Figure 2.2: The scale of the downscaled model grid over Minneapolis and St. Paul, Minnesota. The location of the Minneapolis airport is marked, and the bolded gridcell that includes it provided the data used in this analysis.	70
Figure 3.1: Monthly frequency (percent of total days in each month) of air mass types by location, averaged over 1948-2019.	71
Figure 4.1: Average monthly frequency distributions of air mass categories in the multi-model ensemble under the historical scenario (HIST; 1980-1999).	72
Figure 4.2: As Figure 4.1, but under the mid-century scenario (MID; 2040-2059).	73
Figure 4.3: As Figure 4.1, but under the late-century moderate-emissions scenario (END4.5; 2080-2099).	74
Figure 4.4: As Figure 4.1, but under the late-century high-emissions scenario (END8.5; 2080-2099).	75
Figure 4.5: Average monthly frequency distributions of air mass categories in Minneapolis station observations (1948-2019) and the multi-model ensemble (1980-1999). The TR (Transition) category occurs in the historical record but was not assigned for model outputs.	76
Figure 4.6: Historical multi-model ensemble agreement with JJA monthly temperature averages (°C) in Minneapolis weather station observations in 1980-1999. X-axis and y-axis scales correspond within each plot but not between plots.	77
Figure 4.7: Historical multi-model ensemble agreement with air mass frequency (days per May 20-September 10 season) in Minneapolis weather station observations in 1980-1999. X-axis and y-axis scales correspond within each plot but not between plots.	78
Figure 4.8: Distributions of summer (May 20-September 10) air mass frequency by scenario. Whiskers indicate 1.5 x IQR, with outlying values plotted individually,	

as also applicable to Figures 4.9-4.23. Each observation represents one model-year combination (see Table 4.2 description).	79
Figure 4.9: Distributions of 15:00 air temperatures by scenario, across all summer (May 20-September 10) days and within individual summer air mass types. Each observation represents one day (see Table 4.3 description).	80
Figure 4.10: As Figure 4.9, but for diurnal air temperature ranges between 15:00 and 3:00.	81
Figure 4.11: As Figure 4.9, but for 3:00 air temperatures.	82
Figure 4.12: As Figure 4.9, but for 15:00 dew point temperatures.	83
Figure 4.13: As Figure 4.9, but for 3:00 dew point temperatures.	84
Figure 4.14: Distributions of annual episode frequency of 3 or more consecutive MT+/DT days by scenario, within the May 20-September 10 season. Each observation represents one model-year combination (see Table 4.2 description).	85
Figure 4.15: Distributions of episode durations of 3 or more consecutive MT+/DT days by scenario, within the May 20-September 10 season. Each observation represents one 3+ day episode (see Table 4.2 description).	86
Figure 4.16: Distributions of exceedances of T_{95} on heat wave days by scenario. Each observation represents one heat wave day.	87
Figure 4.17: As Figure 4.16, but including only days within severe heat waves.	88
Figure 4.18: Distributions of annual frequency of positive-EHF heat wave events by scenario. Each observation represents one model-year combination (see Table 4.4 description).	89
Figure 4.19: Distributions of heat wave durations by scenario. Each observation represents one heat wave event.	90
Figure 4.20: Distributions of annual frequency of individual heat wave days by scenario. Each observation represents one model-year combination.	91

Figure 4.21: As Figure 4.20, but counting only days within severe heat waves.	92
Figure 4.22: Distributions of heat wave season lengths by scenario. Each observation represents one model-year combination.	93
Figure 4.23: Distributions of heat wave season starting dates by scenario. Each observation represents one model-year combination.	94

Table of Contents

List of Tables	iv
List of Figures	vi
1. Introduction	1
2. Data and Methods	8
2.1 Station observations	9
2.2 Historical synoptic classifications	10
2.3 Climate model outputs observations.....	13
2.4 Synoptic classifications from model outputs	15
2.5 Air mass trends	17
2.6 Heat wave parameters	19
3. Historical Analysis	23
3.1 Air mass frequency trends	24
3.2 Air mass character trends	25
3.2.1 Overall temperature trends	25
3.2.2 Urban temperature trends by air mass	26
3.2.3 Urban-rural distinctions	27
3.3 Consecutive day analysis	28
3.4 Heat wave behaviors	30
4. Model Output Analysis	33
4.1 Model representation of historical conditions	34
4.2 Air mass frequency trends	37
4.3 Air mass character trends	39
4.4 Consecutive day analysis	41
4.5 Heat wave behaviors	43
5. Discussion	48

6. Conclusion	55
Tables	59
Figures	69
Bibliography	95

Chapter 1: Introduction

Several decades of research have established a critical link between extreme heat and public health. Extreme heat is the leading weather-related cause of human mortality in the United States, exceeding the combined annual mortality rates from other causes such as hurricanes, lightning, tornadoes, and floods (Lee, 2013; Luber & McGeehin, 2008). While heat exhaustion and heat stroke are well-known responses to oppressive ambient meteorological conditions, excessive heat also exacerbates existing vulnerabilities to heart attacks, respiratory failures, and other complications (Anderson & Bell, 2009). Heat-related mortality is typically underreported, as individual instances of death are most commonly attributed to heat only in cases of heat exhaustion or heat stroke, where a causal relationship is more direct. However, these cases represent only a fraction of excess deaths during heat events, and the full extent of the threat posed by heat is better represented by spikes in all-cause above-baseline mortality (Kalkstein & Greene, 1997; Sheridan & Kalkstein, 2004). Age is usually among the most significant risk factors, with individuals over 65 years of age showing the greatest mortality response to heat across a range of geographic conditions (Anderson & Bell, 2009; Basu & Samet, 2002).

Though the associations of mortality, as a binary variable, with extreme heat are generally easiest to quantify, human health responses to heat are highly varied and frequently not life-threatening (Li et al., 2012). During extreme heat events, increases in hospital admissions often extend well beyond the mortality response, as observed in the Chicago heat wave of July 1995, in which over 700 deaths and over 1000 excess hospital admissions occurred (Semenza et al., 1999). However, this Chicago heat event is an unusually well-documented example, while availability of daily time-series data tends to

be insufficient for more comprehensive or widespread studies of heat-morbidity relationships (United States Environmental Protection Agency Office of Atmospheric Programs, 2006). Overall, public perception tends to underestimate the risks associated with extreme heat events due to the lack of physical destruction they leave behind compared to other extreme weather events (Luber & McGeehin, 2008).

Every location has a unique set of sensitivities in the connections between heat and mortality, and several studies have generated predictive algorithms for specific cities or regions (Hayhoe et al., 2010; Sheridan & Kalkstein, 2004). A variety of spatiotemporal factors impact the severity of the mortality or morbidity response to a given heat event. Due to the human body's ability to adjust to heat, the same high temperature conditions will have a lesser impact in a more consistently hot location, such as Arizona, than in a colder or less consistently hot location like Minnesota. Furthermore, a hot day late in a summer season will present less danger than an equally hot day in early summer in the same location due to seasonal acclimatization (Nairn & Fawcett, 2014; Sheridan et al., 2009). Diurnal temperature range is another influential factor in the severity of a heat event, since nighttime cooling can provide relief from a day of excessive heat, and therefore a warmer night following a hot day can exacerbate its adverse health impacts (Vanos et al., 2015). Likewise, days of excess heat are typically most harmful when they occur consecutively; the impacts of heat upon health are cumulative as heat loads build up (Nairn & Fawcett, 2014). Mortality often tends to rise prominently on the third day of a heat event (Anderson & Bell, 2009; Basu & Samet, 2002), and several studies have demonstrated that mortality responses often lag behind peak heat conditions

by 1 or more days (Anderson & Bell, 2009; Hajat et al., 2006; Sheridan & Kalkstein, 2010).

The U.S. Midwest has a particularly strong sensitivity in heat-health relationships due to the high intraseasonal variability of its regional climate, with both tropical and polar synoptic weather regimes exerting a substantial influence throughout most of the seasonal cycle (Kalkstein & Davis, 1989; Sheridan et al., 2009; Sheridan & Dixon, 2017). Several studies have noted a late 20th-century trend in the Midwest of warmer and more humid weather conditions increasing in frequency, replacing more days with cooler and drier conditions (Knight et al., 2008; Sheridan et al., 2009; Vanos et al., 2015). This trend represents part of a more widespread shifting balance in North American weather regimes linked to phase shifts in the North Atlantic Oscillation (Knight et al., 2008).

Since humans acclimatize to location-specific climatological norms, no universal threshold can dictate the presence or absence of heat-stress conditions. Furthermore, human bodies respond physiologically to weather elements, such as temperature, humidity, wind speed, and solar radiation, as an ensemble rather than individually (Kalkstein et al., 1996). Relationships between mortality and temperature alone have been recognized to be non-linear, particularly in the most extreme cases where multiple risk factors compound to produce a deadlier situation (Anderson & Bell, 2009). Therefore, the identification of “weather situations,” based on an ensemble of weather elements, can often delineate the potential for heat-stress conditions more successfully. The Spatial Synoptic Classification (SSC) is one means of doing so, employing a range of single-station surface observations to evaluate synoptic-scale atmospheric circulation patterns (Sheridan, 2002). The SSC categorizes daily weather conditions under a series of

synoptic air mass types, applying location-specific climatological thresholds that shift with the seasonal cycle. This system enables patterns of adverse health outcomes to be tied to specific atmospheric circulation behaviors, in which specific synoptic categories or subcategories may be associated with above-baseline mortality responses. Applications of the SSC to weather forecasts can therefore aid in predicting and issuing warnings for oppressive, health-threatening weather conditions (Hondula et al., 2014; Kalkstein et al., 2011; Sheridan & Kalkstein, 2004). However, the SSC has widespread climatological uses beyond the field of heat and health (Dixon et al., 2016; Hondula et al., 2014). A key advantage of the SSC is its ability to highlight non-uniformities within a changing climate, such as if temperature or other meteorological character changes are concentrated within a certain subset of air mass types rather than being evenly distributed across all days.

Within specific synoptic categories, distinctions in air mass characteristics have been noted between urban and rural locations (Sheridan et al., 2000). Due to the urban heat island effect, urban populations are particularly vulnerable to heat-related mortality. In cities, the built environment absorbs more heat during the day and releases it more slowly at night, raising ambient temperatures in day and even more so at night, and thus depriving residents of nighttime cooling (Harlan et al., 2006). While heat waves are driven by synoptic-scale processes, the urban heat island effect can amplify their impacts locally beyond those received by surrounding rural areas (Fischer et al., 2012; Founda & Santamouris, 2017; Habeeb et al., 2015). Furthermore, particular areas or neighborhoods within urban areas tend to experience the greatest heat stress during heat events, often with correlations to racial and economic disparities (Anderson & Bell, 2009; Gronlund,

2014; Harlan et al., 2006). Thermal heterogeneities within numerous individual cities in the U.S. have been demonstrated to have direct ties to the history of redlining practices (Hoffman et al., 2020; Wilson, 2020). Unequal access to air conditioning is a critical underlying factor in relative risk of heat-related mortality, along with neighborhood disparities in tree cover and quality of construction materials (Harlan et al., 2006).

Many studies have projected the frequency, severity, and duration of extreme heat events in the U.S. to increase throughout the 21st century as a consequence of climate change (Dahl et al., 2019; Hayhoe et al., 2010; Kalkstein & Greene, 1997; Lau & Nath, 2012; Meehl & Tebaldi, 2004). Heat events of comparable severity to the historically unprecedented Chicago heat wave of 1995 may impact the Midwest every other year by end-century even if carbon emissions are substantially reduced, or up to three times a year if emissions remain high (Hayhoe et al., 2010). Meanwhile, heat events exceeding historical precedent are expected to become more commonplace, covering expanding geographical portions of the U.S. but most concentrated in the Midwest, Southeast, and Southern Plains (Dahl et al., 2019; Lau & Nath, 2012). Though the impacts of heat upon health are widely expected to increase in severity due to climate change, such impacts are already observable: over a third of summer-season heat-related deaths that occurred globally between 1991 and 2018 can be attributed to anthropogenic climate change (Vicedo-Cabrera et al., 2021). Human health responses to heat events have actually diminished globally in recent decades due to increased air conditioning saturation, improvements in health care, and in some cases, increased implementation of heat/health warning systems (Arbuthnott et al., 2016; Davis et al., 2002; Sheridan & Dixon, 2017). However, as heat events have become more frequent over the past decade, this has begun

to offset the decreased health outcomes from any individual heat event (Sheridan et al., 2021).

Specifically within Minnesota, observed warming trends are strongest in winter, and this is expected to remain the case throughout the 21st century. However, Minnesota's summers are also projected to warm up to 4°C by the end of the century, with the greatest temperature increases occurring in the northern and central regions of the state (Liess et al., 2021). In light of these climate forecasts, and given Minnesota's susceptibility to heat-related health risks along with other Midwestern states, this study aims to evaluate changing patterns in health-threatening heat conditions in both Minnesota's observed past and projected future. In examining historical synoptic trends, it partially follows the analyses of Midwestern urban centers performed by Vanos et al. (2014), with inclusion of additional urban locations and neighboring rural locations in Minnesota, and under an updated version of the SSC. Utilizing newly available downscaled Minnesota-region climate projections presented by Liess et al. (2021), it examines the continuation of such trends into the middle and late 21st century in Minneapolis, alongside an evaluation of future heat wave behaviors applying a separate, temperature anomaly-based metric for excess heat. The results of the study are intended to be informative to future work in characterizing heat-health relationships specific to Minnesotan cities and alleviating the risks associated with extreme heat.

Chapter 2: Data and Methods

2.1 Station observations

Historical temperature records from four urban and four rural weather stations (Figure 2.1) were downloaded from the Midwest Regional Climate Center (MRCC) climate Online Data Portal. Airport stations in Minneapolis-St. Paul, Rochester, Duluth, and Fargo-Moorhead were selected as urban sites. These represent the four largest metropolitan areas in or partially in Minnesota for which SSC calendars were available. They were also intended to represent the intrastate spatial variability within Minnesota's climate. Jordan, Grand Meadow, Two Harbors, and Ada were paired with these four urban sites respectively as rural sites, in an attempt to capture urban-rural distinctions in air mass character. These sites were selected to be fairly near (35-55 km) to the urban sites to which they were paired, while covering an equivalent period of record, unlike numerous other rural weather stations with more limited records. This meant that rural sites would be presumably close enough to experience the same daily synoptic conditions as their urban counterparts, while simultaneously far enough to avoid any potential urban heat island (UHI) influence. Worth noting, however, are the distinctions in how each airport station is situated relative to its respective urban area. The MSP airport lies within the Minneapolis-St. Paul metropolitan area, aligned with its innermost suburban ring, and has been recognized for the strength of its UHI signal relative to other metropolitan locations outside of the downtown areas of Minneapolis and St. Paul (Smoliak et al., 2015). Meanwhile, the other three airports lie outside or along the edges of their respective built-up urban environments, none of which are as physically expansive as Minneapolis-St. Paul. These urban stations may therefore experience less pronounced

urban heat island effects, thus potentially dampening any urban-rural distinctions that may exist.

Daily minimum and maximum air temperatures were available from 1948 to 2019 in all eight locations, while hourly air temperatures and dew point temperatures were only available from the four urban locations. Therefore, for consistency, daily 24-hour minima and maxima were used in all urban-rural air mass character comparisons. Diurnal temperature range was defined here as each calendar date's maximum temperature minus its minimum temperature, with the acknowledgement that the majority of daily minima precede rather than follow daily maxima. In urban-only synoptic evaluations, consistent 12-hour-interval observations from 3:00 and 15:00 Central Standard Time were applied instead, with the temperature difference between these times functioning as an alternate expression of diurnal temperature range. The use of 12-hour synoptic observations offers more specific insight into the behavior of the diurnal cycle under different air mass types than a reliance on an assumption of minimum temperatures occurring at night or early morning. Given the physiological relief from hot days provided specifically by cool nights, this distinction has important implications for health (Vanos et al., 2015).

2.2 Historical synoptic classifications

The Spatial Synoptic Classification (SSC) categorizes weather situations under a series of air mass types, incorporating surface observations to provide a holistic representation of daily atmospheric conditions over a location (Kalkstein & Greene, 1997; Sheridan, 2002). Single-station observations of air temperature, dew point temperature, cloud cover, wind speed and direction, and pressure at regularly spaced 6-

hour intervals serve as inputs to the SSC algorithm. In heat and health-related applications, the SSC provides a more complete assessment of conditions than traditional metrics of apparent temperature, which factor in a smaller subset of these parameters. The SSC features seven main air mass categories: Dry Polar (DP), Dry Moderate (DM), Dry Tropical (DT), Moist Polar (MP), Moist Moderate (MM), Moist Tropical (MT), and transition days (TR). These categories serve as an extension from the four traditional Bergeron (1930) air mass categories (cP, cT, mP, mT), providing more versatility for health-related and other climatological studies, with greater representation of the modifications that air masses can undergo as they advect over land or water surfaces outside their source regions (Sheridan, 2002). Although they have since been applied globally in climatological studies (Dixon et al., 2016; Hondula et al., 2014), these SSC categories were originally designed to represent North American synoptic circulation patterns; different regions within the continent experience air mass types in widely varying frequency proportions (Kalkstein & Greene, 1997).

Air mass classifications are assigned to each day at a given location through the use of seed days, which exemplify typical weather conditions that each air mass type would bring to that location at a given point in the seasonal cycle. In the previous iteration of the SSC, or SSC2 (Sheridan, 2002), seed days were selected manually based on knowledge of regional climatological norms and with attention to continuity between neighboring stations. From there, the SSC2 automatically matched each day to the category whose seed day for that time of year most closely resembled that day's conditions. The newer SSC3, unlike the SSC2, assigns daily air mass classifications under a fully automated algorithm that selects seed days from the 1981-2010 period to

establish a climatological baseline. In addition to the seven primary synoptic categories, the SSC2 includes a subset of the MT category called MT+, featuring days on which apparent temperatures exceed the local MT seed-day mean by at least one standard deviation (Sheridan et al., 2009). This distinction was created for the purpose of health-related studies, as the MT air mass is too frequent in many locations to be of use in distinguishing daily conditions more likely to result in excess mortality. MT+ thus isolates the hottest and most humid conditions from other milder MT days. The SSC3 expands upon this concept to subdivide other air mass categories in a similar fashion, with all non-moderate types receiving a plus subtype to denote more extreme conditions.

Most studies evaluating the SSC in relation to health outcomes identify DT and MT+ (or the equivalent “extreme” MT subset under SSC1) as “oppressive” heat categories with the strongest associations to excess summer (Kalkstein & Greene, 1997; Sheridan & Kalkstein, 2004; Vanos et al., 2015). These categories represent the hottest summer weather conditions occurring at a given location, distinguished from each other by the relative presence or absence of humidity. Due to their lower dew points, and therefore lower cloud cover and specific heat, DT air masses are typically able to reach the highest temperatures of any synoptic type, while facilitating a wider diurnal range than MT or MT+ air masses. In locations across the U.S. where DT and MT+ both occur and are both deemed as high-risk, primarily east of the Mississippi River, the health risk presented by DT is frequently greatest (Kalkstein & Greene, 1997). The designation of MT+ and DT as oppressive types is not universal, however, and varies from location to location. In regions where MT days are less frequent and MT+ days are especially rare, MT days as a whole may carry a higher heat-related health risk (Kalkstein & Greene,

1997). However, the use of MT+ and DT in representing higher-risk conditions is well-established in synoptic heat-health studies of the Midwest (Hayhoe et al., 2010; Kalkstein & Greene, 1997; Sheridan et al., 2009; Vanos et al., 2015) and is therefore applied here.

Daily SSC calendars were downloaded from <http://sheridan.geog.kent.edu/ssc3.html> for the four urban airport stations. These SSC series offer coverage for slightly differing periods of record between stations, but the period of 1948 to 2019 was included in all four and was therefore used in all analyses. For purposes of this analysis, all “plus” types were aggregated with their “parent” types except for MT+, due to its distinct significance from MT in heat-health studies. Rare cases of even more extreme MT++ days were likewise aggregated with MT+.

2.3 Climate model outputs

A key objective of this study was to assess how the occurrences and characteristics of air masses over Minnesota might change under a variety of future climate change scenarios. To achieve this, simulations of historical and future climate across Minnesota were taken from the downscaled models produced by Liess et al. 2021. Simulated 20th and 21st-century climate conditions were derived from eight general circulation models (GCMs) (Table 2.1), which were dynamically downscaled to a 10km resolution over the Minnesota region through the Weather Research and Forecasting (WRF) model, as detailed in Liess et al. 2021. Each model covers four 20-year scenarios: a historical simulation covering 1980-1999, along with three future simulations covering the middle (2040-2059) and late (2080-2099) 21st century. The late-century period was simulated under both moderate-emissions (RCP4.5) and high-emissions (RCP8.5)

scenarios, while the mid-century period was only simulated under RCP4.5, since the two emissions scenarios diverge less within that time frame. These scenarios will be referred to as HIST, MID, END4.5, and END8.5.

From historical WRF outputs, linear-scaling bias corrections were applied to temperature and precipitation values such that monthly means across each model's 20-year period were consistent with gridded climate normals from PRISM Climate Group (Daly et al., 2017; Liess et al., 2021). These same bias corrections were then applied to future scenarios, under the assumption that each individual model's biases would remain stationary across all scenarios (Teutschbein & Seibert, 2012). Other meteorological variables output from WRF runs, including perhaps most importantly humidity, were not bias corrected in this manner due to the limited availability of observational data across the grid. Bias corrected WRF outputs used in this study had a 1-hour temporal resolution across the model grid. WRF outputs from a single gridcell were selected to represent the location of the Minneapolis airport station (Figure 2.2), in an attempt to represent future continuations of observed trends as directly as possible. Given the coarseness of the 10km spatial resolution remaining after downscaling, no attempt was made to distinguish between urban and rural heat conditions in each of these scenarios. Representation of land cover is limited in both the WRF runs and the GCMs forcing them, and it is outside the scope of this work to predict future urban growth and further changes to land cover resulting from it.

2.4 Synoptic classifications from model outputs

While previous versions of the SSC were primarily designed to categorize historical air masses, the newer SSC3 also facilitates the usage of climate model data as inputs. Synoptic classifications were generated for each day in Minneapolis over each GCM-scenario combination, from air temperature, dew point temperature, sea level pressure, cloud cover, and horizontal wind vectors at 6-hour intervals (3:00, 9:00, 15:00, and 21:00 in local Central Standard Time). Since a key objective of this study was to explore the feasibility of doing so, this portion focused solely on Minneapolis rather than similarly covering the other three urban sites.

Pressure was not available for this study as a direct output of the WRF runs, given its limited usefulness in the downscaled simulations' originally intended applications (Noe et al., 2019). Instead, daily surface pressure anomalies were estimated using a simple linear function of daily mean air temperature, and these anomalies were then added to climate normals provided by the MRCC dataset. Since pressure estimations produced daily rather than hourly values, minor (± 1 hPa) variability was introduced at consistent times of day to provide nonzero daily pressure changes necessary for the SSC algorithm. Cloud cover was likewise unavailable as a direct WRF output and was therefore recalculated from incoming shortwave radiation, expressed as a daily average. Wind direction was unavailable from the downscaled outputs of bcc-csm1-1 and MIROC5 in all four scenarios, along with CNRM-CM5 in the END8.5 scenario. The primary consequence of these data constraints was that the lack of pressure variability within each day, as well as the lack of shifts in wind direction under some GCM-scenario combinations, prevented synoptic transitions from being accurately reflected. As a result,

the TR category was removed from the list of possible synoptic categories for the SSC3 algorithm to assign each day; every day that would have been designated as TR was instead assigned the next-closest-fitting air mass type.

Eight 20-year SSC calendars were produced for each climate scenario, each one derived from a different GCM. This permitted more robust statistical analyses, with 160 model-years per scenario forming a multi-model ensemble, which can be expected to provide more reliable results than those of individual models (Pincus et al., 2008). An attempt was also made to produce a single 20-year SSC calendar generated from an averaged dataset functioning as an alternate expression of the multi-model ensemble, in which all relevant variables were averaged hourly across all eight models before being input into the SSC3 algorithm. However, this latter approach overly moderated the day-to-day meteorological variability relative to observed synoptic behaviors over Minneapolis, resulting in overrepresentation of moderate synoptic types like DM and near-exclusion of rarer and more extreme types like MT+. Under the former approach, SSC calendars were generated from each GCM individually, from which summer air mass frequencies and daily air mass characteristics were averaged afterwards.

As a function of the automated SSC algorithm, each GCM-scenario combination provided its own seed days in the generation of SSC calendars that were used in this study. An alternate approach was also attempted, in which each downscaled GCM provided seed days in its historical simulation that were then applied across all four scenarios. In effect, this meant that the qualifying criteria for classifying any given day as an MT day, or any other category, were identical across all historical and future climate scenarios within each model. Especially in end-century scenarios, this approach resulted

in a more extreme DT takeover of summer months, particularly under CNRM-CM5, MIROC5, and IPSL-CM5A-LR, with partitioning of DT into statistically unrealistic proportions of DT+, DT++, and in some cases even DT+++. The same was true to a lesser extent with MT as with DT, with an oversized MT+ and MT++ presence in some end-century models. This approach also extended DT into winter in some scenarios, an unlikely situation from a synoptic meteorological standpoint. Days meeting current DT temperature thresholds may occur more frequently in future winters, but they are unlikely to be caused by the same circulation patterns associated with DT presence in Minnesota. Similarly, a DT day at a given time of year in Minnesota might more closely resemble a DM day in a warmer location further south, such as Missouri, which could potentially function as an analog for Minnesota's future climate. Therefore, SSC calendars applying the same seed days across all scenarios were not ultimately used in this study. The other approach, which allowed each GCM-scenario combination to set its own climatological baseline, curbed the DT extension into winter and the oversized presence of DT plus types, while redistributing more cooler-end DT days to DM and therefore bringing future average DT temperatures upwards, as addressed in Chapter 4. DT+ and MT++ days still occasionally appeared in these calendars but were aggregated with DT and MT+ days respectively in all analyses, as with historical station-based SSC calendars.

2.5 Air mass trends

Frequency and character changes can occur over time within any synoptic air mass type, but this study focused primarily on four types: DP, DT, MT, and MT+. While DT and MT+ are generally the most oppressive and health-threatening types in the

Midwest, MT is also sometimes associated with above-baseline summer mortality and morbidity. MT is also much more common in the Midwest than DT and especially MT+, and is therefore a climatologically and statistically useful indicator of long-term changes in the relative dominance of synoptic regimes over the region. Trends in DP were assessed alongside the MT, MT+, DT air masses to provide contrast, as DP days may provide particular cooling relief in Midwestern summers from warmer adjacent days (Vanos et al., 2015). An objective was to determine the extent of summer DP replacement by the hotter tropical types, as well as character changes within DP air masses that could indicate whether this cooling relief is becoming diminished.

The summer season was defined as May 20 to September 10 in all analyses of summer air mass character. This was intended to include margins around the typical meteorological summer (JJA) to accommodate the potentially expanding seasonal spread of oppressive conditions under climate change. The range of dates was not expanded further in order to avoid including less relevant or health-threatening days, such as late spring DT days that are unlikely to deliver as much heat as their mid-summer counterparts. All measures of air mass frequency in this study, based on either historical observations or climate simulations, counted the number of days of a given air mass category occurring between May 20 and September 10 each year. Analyses of observed and simulated air mass character trends focused on air temperatures and dew point temperatures at 3:00 and 15:00 within calendar dates assigned a given SSC categorization, except in urban-rural comparisons of diurnal temperature ranges where data availability constraints allowed only the use of daily minimum and maximum temperatures instead.

2.6 Heat wave parameters

A separate, non-SSC-related evaluation of heat wave trends was performed, as a complementary means of assessing changes in health-threatening heat events. While there is no universal standard for defining heat waves, many location-specific heat wave metrics exist (Habeeb et al., 2015; Nairn & Fawcett, 2014; Sheridan & Dixon, 2017; Watts & Kalkstein, 2004), which identify heat events under a different set of criteria than the SSC. They may therefore capture events consequential to health that might not be fully captured by “oppressive” MT+ or DT air mass classifications. For example, the well-documented Chicago heat wave of July 1995 (Hayhoe et al., 2010; Meehl & Tebaldi, 2004) peaked under DT and MT+ conditions from July 12-15, but was extended by additional MT days on July 11, 16, and 17.

In this analysis, heat wave days were determined in accordance with the criteria presented by Nairn and Fawcett (2014), where an Excess Heat Factor (EHF) is assigned for each three-day period. Originating in Australia, the EHF is designed to identify heat events that pose a significant risk to health, reflecting location-specific climatological norms, cumulative impacts of heat, influences of nighttime alongside daytime temperatures, and the effects of acclimatization. Since its introduction, further studies have evaluated its performance in predicting health outcomes, with promising results in Australia and elsewhere (Loridan et al., 2016; Nairn et al., 2018; Scalley et al., 2015). A positive EHF value indicates that the average daily mean temperature (DMT) exceeds the 95th-percentile DMT for a given location (T_{95}). The magnitude of this exceedance of T_{95} (significance index, or EHI_{sig}) is then multiplied by the exceedance of the previous thirty days' average DMT to represent acclimatization (acclimatization index, or EHI_{accl}).

Early-season heat events tend to exceed their preceding weeks' temperatures by greater margins than late-season heat events, and thus often result in the greatest excess mortality outcomes (Nairn & Fawcett, 2014; Sheridan et al., 2009). The EHF is the product of two measures of temperature anomalies, against long-term climatology and short-term weather behavior respectively, and its units are therefore $^{\circ}\text{C}^2$. Any day within a three-day period is counted as a heat wave day even if its individual DMT does not exceed T_{95} . Conversely, a day whose DMT exceeds T_{95} is not counted if it does not fall within a positive-EHF three-day period. The same qualifications apply to severe heat wave days, or days within three-day periods whose EHF exceeds the 85th-percentile EHF value.

Nairn and Fawcett (2014) define DMT as the average of daily maximum and daily minimum temperature. In order to reflect the distinct health impacts of a hot night following a hot day, maximum and minimum temperatures are selected within 24-hour periods beginning and ending at 9:00 rather than midnight, in accordance with Australian weather data formatting conventions. However, they acknowledge the possibility, or even preferability, of using regularly spaced synoptic observations when available, as also utilized in SSC categorization (Sheridan, 2002) and associated analyses (Vanos et al., 2015). In this analysis, DMT was defined as the average of 12-hour temperatures at 15:00 and the following 3:00. This follows the air mass temperature trend analyses outlined above, but reconfigured so that nighttime temperatures follow daytime temperatures rather than aggregating times by calendar date. This was calculated across the periods of record at all four urban stations, for which hourly temperatures were available, and across the periods simulated by each set of WRF runs.

While the EHF formula can also be applied to apparent temperature (Sheridan & Dixon, 2017), it utilizes daily mean air temperature in its original form and in follow-up Australian studies (Loridan et al., 2016; Nairn et al., 2018) to provide greater flexibility across a wider range of observational records. Humidity is intended to be implicit, as both daily minimum and maximum temperatures are factored in, thus reflecting the moderating influence of humidity on diurnal temperature range. This simpler form was applied in this study, since temperatures were bias corrected from WRF outputs, while humidity and wind speed, as applicable to the Steadman formula for apparent temperature (Steadman, 1994), were not. Reducing the potential for multiple biases to compound in the calculation of a secondary metric like EHF was preferable.

From this definition of heat wave days, heat wave season length was defined as the duration from each year's first heat wave day to its last, as applied by Habeeb et al. (2015) with somewhat different heat wave criteria. The timing of each year's heat wave season was also expressed as the Julian day upon which the first heat wave day falls. Because of differences in acclimatization, a heat wave season encroaching earlier into late spring has greater health implications than a heat wave season continuing later into early fall, for instance. This is reflected in the EHF's acclimatization component but not its significance component, whose sign determines the presence or absence of a heat wave to begin with (Nairn & Fawcett, 2014).

For each year, heat wave intensity was expressed as mean exceedance of T_{95} on heat wave days. In a more variable summer climate, greater temperature excursions are required for a heat wave to qualify as severe than in a more stable, low-variability summer climate. To address this, severe heat wave intensity was expressed likewise as

mean exceedance of T_{95} . Heat wave duration was defined as the average number of heat wave days occurring consecutively per heat event, regardless of whether all of them exceed T_{95} individually, while heat wave frequency was defined as the number of these events per year. These definitions were applied equally to hourly station records from the four urban locations and to hourly WRF outputs representing Minneapolis.

Chapter 3: Historical Analysis

3.1 Air mass frequency trends

The four urban locations examined in this study (Minneapolis, Rochester, Duluth, and Fargo) are comparable in their overall relative balance of synoptic regimes over the seasonal cycle. All of them experience both polar types and both moderate types throughout an average year, with DP and MP peaking in winter and DM and MM peaking in summer (Figure 3.1). DT and MT are present from March to November, though to varying degrees. DT tends to peak in spring, though still never exceeding 8% of any month's days in an average year. MT is far more common in all locations, especially in summer, with occasional MT+ occurrences in May through September. Transition days occur about 10-15% of the time in each location throughout the entire year.

While these patterns hold true for all four stations, some distinctions are present, particularly between the two northern and two southern sites. DP air masses are more dominant overall in winter and more persistent through summer in Fargo and Duluth than in Minneapolis and Rochester (Figure 3.1). Fargo's MP occurrence patterns are more comparable to the southern cities, where MP displays less presence in winter and more concession to MT in summer. Meanwhile, Minneapolis and Rochester exhibit nearly identical seasonal behaviors, with a slightly less negligible MT+ presence in Minneapolis. It is worth noting that all these represent average seasonal cycles, while the occurrence frequency of each air mass type is highly variable between individual years.

These generalized patterns have held true over the entire period of record, but from 1948 to the present, air mass frequency patterns have shifted. MT days have experienced a statistically significant increase in summer frequency in all four cities,

ranging from an average decadal increase of 1.0 per summer in Fargo to 1.8 per summer in Rochester. In all cities except Rochester, the MT frequency increase has occurred alongside a DP frequency decrease, which was statistically significant in Minneapolis and Duluth (Table 3.1). This is consistent with trends observed in previous synoptic studies of the Midwest (Knight et al., 2008; Vanos et al., 2015).

Several other air mass types, to which this study focuses less attention, have also experienced frequency shifts in Minnesota. TR frequency has roughly halved in all locations over the period of record, aligning with a more geographically widespread downward trend (Kalkstein et al., 1998; Knight et al., 2008), while DM days have shown statistically significant increases in Duluth and Fargo. MP days have undergone a smaller frequency reduction in all locations, with statistical significance in Duluth, the location in which they have the greatest presence in summer.

3.2 Air mass character trends

3.2.1 Overall temperature trends

Daily summer maximum temperatures underwent minimal changes across all locations, with no statistically significant trends except for a 0.14°C decadal increase in Duluth and a 0.18°C decadal decrease in Ada. Meanwhile, daily summer minimum temperatures increased in all locations except Grand Meadow, with statistically significant upward trends of 0.19°C or more per decade in all urban locations as well as Two Harbors. This effect was strongest in Minneapolis, followed by the urban-rural pair of Duluth and Two Harbors, with 0.30°C, 0.28°C, and 0.24°C decadal changes respectively.

These two sets of trends resulted in a narrowing of the diurnal temperature range in all locations, with statistical significance everywhere except Jordan and Grand Meadow (Table 3.2). This narrowing was greatest in the two southern urban locations and the two northern rural locations, while occurring to a lesser extent in their respective adjacent counterparts.

In addition to temperature changes, nighttime and daytime dew point temperatures experienced changes over the period of record, though these data were only available for the urban locations. Both 3:00 and 15:00 dew points, averaged across all summer days, increased by 0.1°C to 0.25°C per decade in all locations. These trends were statistically significant in all cases except for 3:00 dew points in Duluth and 15:00 dew points in Minneapolis. A net gain in vapor content aligns logically with the observed increase in prevalence of MT air masses, the most humid category, at the expense of DP, the driest and typically coolest category.

3.2.2 Urban temperature trends by air mass

Breaking down these temperature and dew point trends by synoptic categories reveals that these changes did not occur uniformly over all air masses (Table 3.1). MT afternoon temperatures actually decreased over the period of record, with statistical significance in all urban locations except Minneapolis. MT nighttime temperatures exhibited an upward trend in all four cities, with significance in Minneapolis only. MT air masses additionally gained nighttime humidity in Minneapolis and Rochester, and daytime humidity in Rochester even as daytime air temperatures decreased. MT+ air masses were too infrequent for significant character changes of their own to be evaluated

in any of the cities. DT days showed no significant temperature or dew point trends in any of the four cities, aside from a downward shift in afternoon DT dew points in Rochester. Meanwhile, DP air masses featured nighttime warming in all four, along with increased nighttime and daytime dew points in Rochester and Fargo.

3.2.3 Urban-rural distinctions

Overall, distinctions between urban sites and their rural counterparts suggest a greater potential for growing urban heat island influence in the two southern pairs than the two northern pairs. Jordan and Grand Meadow were the most frequent exceptions to diurnal range narrowing patterns within specific synoptic categories and across all days, showing significant narrowing only within DP days (Table 3.2). Grand Meadow was also the only location to feature a significant nighttime cooling trend in either DT and MT air masses. MT+ days had a downward nighttime temperature trend in both Jordan and Two Harbors, though MT+ days are extremely rare, only occurring at all in a minority of years in Two Harbors and only more than once within five years. DP diurnal ranges grew narrower in all locations except Fargo, one of only two cases in which this occurred for a rural site but not its paired urban site within a given air mass type; the other was a DT diurnal range narrowing in Two Harbors but not Duluth. Overall, out of the four air mass types specifically examined, DT showed the least consistency, with only half of the sites experiencing a statistically significant narrowing effect on DT days: Minneapolis, Fargo, Two Harbors, and Ada. No significant increases in the diurnal temperature range occurred within any SSC type in any of the eight locations examined.

Most significant decreases in the diurnal range, largely within DP and MT, were primarily driven by nighttime warming, where daytime cooling was either lesser in magnitude or statistically insignificant (Table 3.1). This pattern held less consistently in rural locations than in urban locations. In cases where the diurnal temperature range decreased for both paired locations under the same air mass, negative regression slopes were generally steeper in the urban site. All exceptions to this pattern, other than Minneapolis and Jordan under DP air masses by a narrow margin, occurred within the two northern pairs of sites.

Over the period of record, the average magnitudes of these diurnal ranges were mostly lower in the urban sites. This held true across all air masses over Minneapolis and Jordan, where the greatest discrepancy was expected, while Duluth and Two Harbors provided the most exceptions. In all exceptions other than DP days in the Duluth area and DT days in the Rochester area, urban diurnal ranges exceeded their rural counterparts' diurnal ranges by less than 0.5°C.

3.3 Consecutive day analysis

Since multiple days of oppressive heat conditions exert a cumulative impact on health (Anderson & Bell, 2009; Hajat et al., 2006; Nairn & Fawcett, 2014), consecutive days of DT and MT+ were examined as one means of evaluating this effect. Consecutive occurrences of 3 or more summer days under either DT or MT+ air masses were identified over the periods of record of all four urban sites, as performed by Vanos et al. (2014) over a wider array of Midwestern cities under a previous version of the SSC. As in previous analyses, the extremely rare DT+ and MT++ days were grouped with DT and

MT+ respectively. While some hotter MT days falling short of the MT+ designation can still present health complications, MT days as a whole are too common throughout Minnesota and the Midwest to serve as a useful oppressive air mass category. The much greater relative frequency of MT also lends itself to longer consecutive runs. Therefore, trends in runs of 3 or more oppressive air mass days, with MT included, tended to effectively mirror the trends in overall MT frequency as outlined above.

No statistically significant regression trends were found in the frequency of these 3+ day episodes (Table 3.3); at least half of all years in all locations included no such episodes at all in the summer season. Nonetheless, a clear contrast between the locations was highlighted. Duluth, where DT is especially rare in summer and MT+ is virtually nonexistent, only experienced 11 consecutive DT/MT+ episodes over the entire period, with 1961 as the only year including two of them. Minneapolis experienced the most, with 61 total episodes, including 15 years featuring two or more and reaching a maximum of six episodes in the summer of 1976. Rochester and Fargo experienced 29 and 49 episodes respectively. Minneapolis's consecutive runs grew significantly longer in the years in which they occurred, with annual mean duration increasing from 3.4 to 5.0 days per event by linear regression. The other cities, all of which experienced more summers with no such events than Minneapolis, displayed downward trends in episode length instead (Table 3.3). The longest recorded summer episodes in Minneapolis and Rochester lasted 9 days each, occurring in 2012 and 1955 respectively. Fargo's longest episode within the seasonal limits of May 20 to September 10 lasted 8 days, but actually began on May 18, 1980 for a total of 10 days. Meanwhile, Duluth's longest episode was only 5 days, also occurring in late May of 1980.

3.4 Heat wave behaviors

Heat waves, as defined by Excess Heat Factor (EHF) criteria, are extremely variable in their year-to-year occurrence in Minnesota. As a result, virtually no patterns in heat wave frequency or characteristics exhibited trends with statistical significance (Table 3.4). Even the length of the heat wave season was highly variable, with some years featuring only a single three-day heat wave or none at all, while the longest season lasted 131 days in both Minneapolis and Rochester in 1959. Across the period of record, the average heat wave season spanned from late June to mid-August in all four locations. Duluth's heat wave seasons lengthened by 2.9 days per decade at $p < 0.1$ significance, while lesser, non-significant ($p > 0.1$) increases in season length also occurred in Minneapolis and Fargo.

Due to the relative nature of the EHF, being based on exceedances of a location-specific 95th-percentile daily mean temperature threshold, few distinctions were present between the heat wave behavior patterns of each location. This suggests that intraseasonal temperature excursions behave comparably across Minnesota. However, Duluth's T_{95} threshold was lowest at 21.6°C, with thresholds of 25.8°C, 24.2°C, and 24.7°C in Minneapolis, Rochester, and Fargo respectively. Between all four locations, heat waves lasted an average of 5.0 to 5.7 days and occurred an average of 3.5 to 4.0 times per year, totaling 20 to 22 days in an average season. The longest heat wave per year ranged on average from 7.5 days in Fargo to 8.9 days in Rochester. Only two years in Duluth featured a heat wave lasting 15 days or more, and only three in Fargo; meanwhile, Minneapolis experienced six such years and Rochester experienced ten. Duluth experienced a significant ($p < 0.05$) increase in annual maximum heat wave

duration, with an average decadal increase of 0.4 days per event, while also adding 1.3 heat wave days to the season per decade ($p < 0.1$). Variability between years was too high for clear upward or downward trends to be observed likewise in the other three cities.

A breakdown of EHF heat wave days by SSC categorization revealed that these heat waves did not occur exclusively under “oppressive” DT or MT+ days (Table 3.5). Though not every day exceeding the 95th daily mean temperature percentile individually is counted as a heat wave day, this is nonetheless unsurprising in locations where DT and MT+ collectively represent less than 5% of summer days. Across all heat wave days in each location, MT was the most represented air mass, ranging from 37% of heat wave days in Fargo to 49% in Rochester. DM was the second most represented in all cities except Minneapolis, where it came in a close third behind DT. TR days accounted for 7-10% of heat wave days in all four locations. Even MM, typically not a particularly warm type, covered 10% of them in Duluth, where the traditional oppressive MT+ and DT types were least frequent and thus left most EHF-based heat wave days open to other air masses. When examining severe heat wave days only, MT+ and DT were better represented, especially in Minneapolis where they collectively covered 62% of such days, with MT making up most of the remainder. MT+ and DT accounted for roughly half of all severe heat wave days in both Rochester and Fargo, though less than a quarter of them in Duluth, where nearly half were still MT and most of the rest were DM. Overall, this superimposition of the two primary heat identification methods used in this study highlighted the distinctions between the two and what purposes they serve. While both can fulfill roles in heat-health studies, the EHF is based on a single weather element, temperature, while the SSC is specifically intended not to do so. Consecutive-day heat

behaviors are built into the EHF, allowing it to capture longer-lasting heat events in which MT or DM days may interrupt runs of DT and MT+ days categorized individually.

Chapter 4: Model Output Analysis

4.1 Model representation of historical conditions

While Chapter 3 examined historical trends in air mass frequency and character in Minneapolis and three other cities, along with rural sites adjacent to each city, this portion of the study focused on future air mass trends in Minneapolis as simulated by an ensemble of downscaled GCMs. In addition to three future climate scenarios, the GCMs covered a historical scenario to facilitate direct comparisons of Minnesota's future climate to its past climate. Before applying equivalent methods to assess future climate conditions in this study, the performance of the model in replicating the behaviors of synoptic air masses over Minneapolis was evaluated.

SSC calendars were produced from each of the eight downscaled GCM outputs utilized in the study. While the patterns of air mass occurrences throughout the season cycle varied considerably across the eight models under all four climate scenarios (Figures 4.1-4.4), the historical multi-model ensemble provided a better representation of observed historical conditions better than most individual models. When monthly frequencies of each air mass type were averaged across the models, some discrepancies from station observations remained (Table 4.1, Figure 4.5). Most notably, the absence of the TR category in the model-derived SSC calendars led to roughly a 10-15% amplification of the collective frequency of all other categories throughout each month. Even without TR, though, relative proportions of the other categories showed some bias in the multi-model ensemble. MM and MP were notably overrepresented throughout the seasonal cycle, but most strongly outside of the summer months upon which this study focused. In summer, DT days were overrepresented in the ensemble by more than double, while MT days were underrepresented and the already rare MT+ days were roughly

halved in frequency. DP was underrepresented throughout the entire seasonal cycle, also roughly halved in summer frequency and virtually eliminated altogether during summer under some individual models, generally those maintaining a stronger summer MP presence instead (Figure 4.1).

Aside from overall summer frequency biases, a notable model-observation discrepancy was apparent in the timing of air mass frequency peaks, as the months in which DT and MT types respectively peaked roughly switched (Figure 4.5). North American atmospheric circulation patterns are most favorable to the presence of DT air masses in Minnesota in spring and early summer, while southerly flow tends to bring MT and MT+ air masses to the region most strongly in mid to late summer. Nearly the opposite occurred in the historical multi-model ensemble: DT featured most strongly in July and August, while MT was most common in May and June, and MT+, though still rare across all months, was mainly restricted to spring. The overall balance of moist and dry types further revealed a bias in the multi-model ensemble toward more humid conditions in spring and early summer, which continued into the future scenarios. These results align with the findings of Liess et al. (2021) that most of the change in future statewide precipitation can be expected to occur in spring and early summer.

While monthly SSC frequency averages from the 1948-2019 observation record better represent the longer-term seasonal synoptic trends typical for Minneapolis, the historical downscaled GCMs were specifically intended to replicate the distinct conditions of the late 20th century. Station observations from 1980 to 1999 were not always representative of longer-term frequency patterns. DT days were particularly infrequent in summer months during these two decades outside of 1980 and 1988, two

distinct years in much of the U.S. for both extreme heat and drought, especially the latter in the Upper Midwest (Lyon & Dole, 1995; Minnesota Department of Natural Resources, 1989). Therefore, model-observation discrepancies in summer DT frequency were amplified when only these 20 years of observations were included: this subset of the record featured 4.7 DT days per average summer rather than 6 over the full record, in comparison to the models' 13 (Table 4.1). MM's seasonal average frequency was 2 days higher across just 1980-1999 than across the full record, while DP's was 1.5 days higher and DM's was 3.3 days lower; all other types differed by less than 1 day per summer in this regard. Thus, under this shorter set of observations, the model-observation frequency discrepancy was reduced for MM and amplified for DP and DM.

A comparison of the historical model ensemble mean and the equivalent 20-year period of observations revealed greater year-to-year variability in the observational series among monthly temperature and dew point averages alongside air mass frequencies (Figures 4.6-4.7), though this may stem from the fact that each model year represented an average of all eight models. Nighttime dew points across all air masses were lower on average in the model ensemble than observations in June, July, and August (Table 4.1). Meanwhile, the models overrepresented daytime dew points in June, and underrepresented them in July and especially August. This aligns with the discrepancies observed in the timing of seasonal frequency peaks in DT and MT, and overall balance of dry and moist types, relative to observation-derived SSC calendars (Figure 4.5).

In all three summer months, the models represented air temperatures somewhat more accurately than dew points, with no discrepancies in monthly averages exceeding 1°C (Table 4.1). However, in spite of the bias corrections performed, temperature

discrepancies were still present. Temperature bias corrections were based on grid-interpolated rather than single-station observations, and focused on average overall daily temperatures within each month rather than two specific times of day as examined here. Simulated nighttime temperatures were warmer than observations in all three months, while simulated daytime temperatures were slightly cooler than observations in June and slightly warmer than observations in July and August. The narrowing of June diurnal temperature ranges by roughly 1°C in the model ensemble aligns with the ensemble's overestimation of both daytime and nighttime dew points in June.

4.2 Air mass frequency trends

Taking note of the model-observation discrepancies in summer air mass occurrences over Minneapolis, 21st-century changes in air mass frequency were evaluated through comparison of future simulations to historical simulations. SSC calendars generated from the four simulated climate scenarios demonstrated a clear 21st-century shift toward more frequent tropical air mass types and less frequent polar types. Monthly air mass frequencies in the multi-model ensemble across the seasonal cycle showed only minor changes in the relative balance of dry and moist air masses, mostly in winter months where moist-category days began to slightly outnumber dry-category days. In summer months, DT had the greatest net gain in frequency over the 21st century under both moderate and high conditions, while DM had the greatest net loss (Table 4.2, Figure 4.8). However, DM remained the most common summer air mass except under END8.5, where it was narrowly outnumbered by MT.

The multi-model ensemble showed the emergence of DT as a more dominant synoptic pattern in Minnesota summers by the end of the 21st century, particularly under higher emissions. In both END4.5 and END8.5 simulations, it replaced MM among the three most frequent summer air masses alongside DM and MT (Table 4.2). Though overrepresented already in the historical simulations relative to the observed record, it doubled in average summer frequency from HIST to END8.5, increasing by over 60% even under END4.5. While falling short of exceeding MT frequency in an average summer even in END8.5, DT showed much more year-to-year and model-to-model variability in frequency, with the greatest standard deviation among model-years of any air mass in future simulations. Two END8.5 model-years, both from the MIROC5 model, included over 90 summer DT days, thereby covering the vast majority of the season (Figure 4.8). DT's frequency increases were relatively proportional within the months in which it already occurred under HIST, with almost no expansion beyond the March-October range it already occupied (Figures 4.1-4.4). Under all scenarios, it continued to peak in frequency in July and August, maintaining its late-season bias relative to Minneapolis historical observations. Contrary to DT, DP days were already underrepresented in simulated historical summers and diminished further in summer frequency in future simulations, with statistical significance by the end of the century. Most models nearly or even completely eliminated DP from July and August under the END8.5 scenario, while substantially weakening its presence throughout the rest of the year.

While none of the dry synoptic types showed significant summer frequency differences between HIST and MID, MT displayed a stronger mid-century increase in

frequency (Table 4.2, Figure 4.8). This increase roughly counterbalanced the amount to which observed MT frequencies were underrepresented in the HIST scenario to begin with. Under RCP4.5 simulations, average MT frequency was actually slightly lower at the end of the century, and under RCP8.5 was higher than mid-century by much smaller margins than for DT. MT+ days became more frequent in future simulations, increasing from 1 per summer under HIST to over 5 per summer under END8.5, taking very nearly the reverse of the DP frequency trajectory (Table 4.2). In both end-century scenarios, MT gained a minor presence in winter and an amplified presence in all other months, widening its seasonal distribution around a consistent June peak (Figures 4.3-4.4). Likewise, MT+ expanded into earlier spring, later summer, and fall while continuing to feature most prominently in April through June.

4.3 Air mass character trends

Since each model run was intended to collectively represent a period of time rather than individually representing specific years, some inter-scenario comparisons in this study removed the aggregation of events by year. This was applicable to all analyses of air temperature and dew point temperature behaviors outlined below, as well as the durations of consecutive runs of MT+ and DT days. Leaving all days of a given air mass type unaggregated prevented individual events from carrying more statistical weight in years where fewer such days occurred, and improved the performance of most t-tests evaluating statistically significant differences between model scenarios. This differs from the analyses presented in Chapter 3, where all variables were aggregated into yearly averages in order to facilitate time-series linear regressions. Seasonal frequencies of air

mass types or consecutive runs are inherently one-value-per-year variables, and were therefore treated identically between observation-based and simulation-based analyses.

In future scenarios, average 15:00 temperatures across all days increased more than 15:00 temperatures within any individual air mass (Table 4.3), with increasingly frequent MT and especially DT days carrying greater weight in bringing up the overall average. In addition to showing a larger frequency increase than MT, DT days also increased further in average 15:00 temperatures than MT, especially by end-century (Figure 4.9). In the END8.5 scenario, DT daytime temperatures displayed a greater standard deviation than any other air mass except DM. This suggests that as DT is forecast to become a more frequent air mass over Minneapolis, the differences in relative risk of mortality between a hotter DT day and a cooler DT day may become increasingly relevant.

MT+ remained relatively infrequent throughout all scenarios, so fewer of its character changes were statistically significant, but it largely followed the same trends as MT. Both nighttime and daytime dew point temperature differences between MT and MT+ days narrowed, with increased MT humidity reducing the gap to less than 1°C in both end-century scenarios (Table 4.3). However, MT+ maintained a 3.0-3.5°C air temperature margin over MT in the daytime through all scenarios, and a 3.5-3.9°C temperature margin at night.

DP showed the least significant character change between HIST and MID out of all air mass categories, with the bulk of its temperature and humidity increases instead occurring between MID and the end-century scenarios (Table 4.3). Minimal differences

were present between the two end-century scenarios in DP daytime temperatures or dew points, though END8.5 featured warmer DP nights than END4.5.

At mid-century, most non-oppressive air masses displayed a statistically significant change in diurnal temperature range, as expressed here by the temperature difference between 3:00 and 15:00 within calendar days, across the simulated scenarios. Diurnal temperature ranges widened from HIST to MID, with $p < 0.05$ significance across all days and within DM, MP, MM, and MT days, then narrowed under both end-century scenarios (Table 4.3, Figure 4.10). END4.5 and END8.5 featured very similar diurnal ranges overall and across most individual air masses, though both nighttime and daytime temperatures were 2°C lower in END4.5. From MID to END4.5, overall average daytime temperatures actually decreased by 0.4°C, while average nighttime temperatures increased by 2.1°C (Figure 4.11). Meanwhile, both nighttime and daytime dew point temperatures increased by 1.2-1.5°C from HIST to MID and changed minimally between MID and END4.5 (Figures 4.12-4.13). Under END8.5, this increase in dew points grew to 2.8°C from HIST. This change was distributed somewhat unevenly across individual air masses, with more mid-century increases in humidity under moist categories, while dry categories, especially DP, reserved their most significant increases for end-century (Table 4.3). The difference in moisture content between DT and MT was therefore greater under MID than any of the other scenarios.

4.4 Consecutive day analysis

As was performed in Chapter 3 for the four cities' historical records, the occurrence of consecutive MT+ and DT days, representing the oppressive air mass types

most associated with excess summer mortality in the Midwest, was examined for 21st-century Minneapolis. The multi-model ensemble featured more MT+ and DT days by mid-century, though only at $p < 0.1$ significance for DT, and even more by end-century under both RCP4.5 and RCP8.5 emissions scenarios. Unsurprisingly, this resulted in more regularly occurring episodes of 3 or more such days falling consecutively. All future scenarios featured a significant increase in episode frequency, more than doubling from HIST to END8.5 (Table 4.2, Figure 4.14). This closely matches the approximate doubling of DT frequency between those same scenarios; DT days remained far more common than MT+ days in every scenario and therefore contributed to the bulk of these consecutive episodes. Tails of episode length distributions grew longer with time and under higher emissions (Figure 4.15), but except under RCP8.5, changes in average episode length were minimal and statistically insignificant.

It should be noted that due to the historical model bias toward higher summer frequency of both MT+ and DT days, historical simulations likewise overestimated how often they occurred for 3 or more consecutive days. Across the Minneapolis period of record, the observed average summer experienced 0.8 consecutive episodes, while the historical model ensemble featured 1.8 per summer in an average model-year. The longest consecutive summer episode recorded in Minneapolis lasted 9 days, and the mean duration across the period of record was 4.2 days. Meanwhile, in the historical model ensemble, the average duration was 5.3 days, with a few instances in some models exceeding 20 days. In contrast, the END8.5 scenario included 18 episodes exceeding 20 days. The longest two, both from CNRM-CM5, exceeded 50 days, spanned most of July and August, and included almost exclusively DT rather than MT+ days. MIROC5 alone

contributed 9 of the other 16 longest consecutive episodes. Though such long-lasting events contributed to the higher average duration in END8.5, shorter episodes remained common, with the majority still occupying the 3-day to 7-day range (Figure 4.15).

4.5 Heat wave behaviors

As in Chapter 3, the Excess Heat Factor (EHF) provided an additional metric, alongside the SSC, by which the future occurrence of consecutive days of excess heat in Minneapolis could be evaluated. In Minnesota and beyond, climatological shifts are expected to become more drastic in the 21st century than from the mid-20th century to the present, regardless of emissions scenario. In this study, this was reflected in the heightened presence of extreme heat conditions as defined both through SSC oppressive air mass occurrences and EHF heat wave events. However, much depends on the extent to which residents of the Minneapolis area are able to acclimatize to overall hotter temperatures in the long term. This form of acclimatization is distinct from the short-term intraseasonal acclimatization that the EHF is specifically designed to address. Therefore, EHF-based heat waves in future scenarios were evaluated in two ways: either by applying the same T_{95} threshold from historical runs across all projected runs within each model, or allowing each individual model run to provide its own, typically higher, T_{95} threshold. Temperature thresholds above which excess mortality becomes more likely vary by location-specific climatology (Curriero et al., 2002), but the transfer of this concept to the same location under a changed climate has proven challenging to address (Kinney et al., 2008). These two forms of heat wave assessment could be interpreted as “no acclimatization” and “full acclimatization” respectively, implying two extremes of

mortality response to heat, between which an intermediate or “partial acclimatization” response is more likely.

In future scenarios, 95th percentiles of daily mean temperature demonstrated a clear increase, by as much as 4.6°C by end-century under RCP8.5 (Table 4.4). Under the application of each model’s historical T₉₅ threshold to qualify future heat events, these events must achieve a higher EHF value to count as severe. The increases in this threshold were uneven across the eight models, as indicated by the increased standard deviation of T₉₅ values across the model ensemble. Likely due to the temperature bias corrections applied previously, the historical models’ average T₉₅ was only 0.5°C greater than that of Minneapolis station observations (Table 3.4). However, the historical models’ average EHF₈₅ severity threshold was 4.6°C² lower than that of observations, potentially indicating a slightly lesser degree of intraseasonal summer temperature variability represented in the model ensemble. EHF₈₅ severity thresholds grew higher in all “no-acclimatization” future scenarios, as exceedances of historical T₉₅ thresholds became more commonplace and necessitated that the top 15% must exceed them by greater margins. However, the same pattern did not hold when each scenario’s own T₉₅ threshold was applied in the identification of heat waves. Under such “full-acclimatization” heat wave criteria, EHF₈₅ only increased in mid-century, instead decreasing slightly in both end-century scenarios. This corresponds with future severe heat wave days’ exceedances of their own scenarios’ respective T₉₅ thresholds, which increased in MID and decreased in END8.5 (Table 4.4). Though this might suggest a lack of increased summer temperature variability in Minneapolis as its warming progresses, the EHF₈₅ threshold is not intended primarily as a climatological indicator of summer

variability, but instead as a predictor of the conditions most likely to produce severe health outcomes.

Since the exceedance of T_{95} on each heat wave day was counted individually, in order to avoid double or triple-counting middle days of longer heat waves, some negative T_{95} exceedances were present across all scenarios. As noted previously, it is fully expected that some days within positive-EHF three-day periods will not themselves individually exceed T_{95} . In historical and mid-century scenarios, these “negative-exceedance” days amounted to over a quarter of heat wave days (Figure 4.16). Such days were even present, though at much lower rates, within severe heat waves in all four scenarios (Figure 4.17) implying that they occurred directly alongside substantially hotter days. This consideration of individual days’ T_{95} exceedances is comparable but distinct from the significance component (EHI_{sig}) of the EHF, which addresses the mean exceedance of T_{95} over a three-day period as a whole, thereby qualifying an event as a heat wave in the first place.

Across all heat wave parameters examined, significant changes were present between model scenarios under the consistent application of historical T_{95} thresholds (“no acclimatization”), while virtually no distinctions were present when each model run’s individual T_{95} threshold was applied instead (“full acclimatization”). Due to the inherently relative nature of the EHF, this is unsurprising, since by necessity the top 5% of daily mean temperatures will occur on roughly 18 days, or 5% of an average year.

When the same heat wave thresholds (“no acclimatization”) were applied across all scenarios within each model, the frequency of heat waves per season nearly doubled from HIST to END8.5, reaching an average of 6 events per year (Figure 4.18). These

events also nearly doubled in duration, reaching an average of 11.6 days. Most of the frequency increase was already present by MID, from which no further increase occurred between MID and END4.5. Across all scenarios, the distributions of heat wave durations showed strikingly long tails, with at least one model featuring an event lasting over 40 days (Figure 4.19). These patterns align with the findings of Dahl et al. (2019) projecting increases in frequency and duration of heat events exceeding fixed heat-index-based thresholds across the U.S. These frequency and duration increases in future models compounded to result in the number of annual heat wave days more than doubling in MID, nearly tripling in END4.5, and nearly quadrupling in END8.5 (Figure 4.20). Severe heat wave days also increased in number at similar ratios, more than quadrupling in END8.5 (Figure 4.21).

“No-acclimatization” heat wave season length increased under all future simulations and more than doubled under END8.5, with more 3-day exceedances of the historical T_{95} occurring both earlier and later in the year. The shortest nonzero-length heat wave season under END8.5 was much longer than the average heat wave season under HIST (Figure 4.22). Under END8.5, the average starting date of the heat wave season shifted backward from late June to late May, with none beginning later than late June in any model-year combination (Figure 4.23). Meanwhile, “full acclimatization” heat wave seasons maintained nearly identical starting dates and showed no statistically significant lengthening or shortening across scenarios (Table 4.4). This indicates that the hottest 5% of annual weather conditions can be expected to continue occupying the same overall time frame within summer rather than becoming biased earlier or later in the year. This consistency within the seasonal cycle across scenarios aligns with the consistency of

monthly ranges in which hotter air masses, especially DT, are projected to occur (Figures 4.1-4.4), although at increasing frequencies within its monthly range. This study did not examine future allocations of air mass types on positive-EHF days, but as DT is projected to grow dramatically in frequency, occur more regularly in consecutive stretches, and expand its margin above MT+ as the hottest air mass type, it is expected to be particularly well-represented within heat waves.

Chapter 5: Discussion

Historical trend analyses indicate a frequency increase in hotter and more humid summer days at the expense of cooler and drier ones, further demonstrating what prior studies have shown for the Midwest and elsewhere (Knight et al., 2008; Vanos et al., 2015). Thus far, the MT weather type has increased more than the DT weather type in both frequency and temperature; overall non-uniformity of temperature trends across air mass types is a key takeaway from this study. Each air mass type forms in different geographic regions under the influence of different circulation patterns, not all of which can be expected to change equally in a warming climate. Since dry heat (DT) and humid heat (MT and MT+) produce different physiological responses among humans, and may raise different relative risks of mortality within distinct age demographics, these trends carry important implications for public health in Minnesota's urban areas.

Differences in results between the locations examined indicate that despite the large scale of synoptic air masses, the whole of the Minnesota region does not experience heat events equally. By some SSC and EHF-based evaluations, the southern cities of Minneapolis and Rochester are more frequently prone to oppressive heat conditions than the northern cities of Fargo and Duluth. Under other measures, such as frequency and temperature characteristics of DT, Fargo more closely resembles the southern cities than Duluth. Fargo and Duluth share comparable latitudes, but DT and MT+ occur at Minneapolis-like frequencies in Fargo while remaining extremely rare in Duluth, likely due to a lake cooling that modifies these air masses into more benign types as they approach Lake Superior. Fargo's location to the west of the other three cities may also grant it more direct access to warm and dry westerly or southwesterly advection from the Great Plains.

The widening of urban-rural distinctions over the period of record suggests a greater urban heat island influence than climate change influence, at least in the two southern urban-rural pairs, though the format of this study is insufficient to confirm this. Given the greater magnitude in projected future warming patterns observed by Liess et al. (2021) in northern Minnesota than southern Minnesota, it is possible that such patterns are already in effect, thus leaving the southern rural sites least affected by either warming influence. Meanwhile, the model-based portion of this study specifically addresses climate change, but does not account for thermal modifications of air masses at the urban or intra-urban scale, due to the spatial limitations of the WRF model outputs.

Climate projections of Minnesota's future demonstrate an acceleration of observed warming trends, but the synoptic trends they forecast do not merely represent a continuation from those of the previous seven decades. Instead, a more complex set of developments could be expected. The DT air mass best exemplifies this, as it has not historically shown significant increases in either frequency or temperature, yet its future frequency and temperature increases are among the most dramatic changes depicted by the multi-model ensemble. Already one of the most oppressive and health-threatening weather types in Minnesota and the Upper Midwest, DT is essentially guaranteed to become a more regular occurrence by the end of this century, whether or not future carbon emissions are reduced. However, the increasing abundance of summer DT days raises the question of whether DT is likely to remain a useful indicator of health-threatening conditions, as does the increased variability in 15:00 temperatures among DT days under END8.5. If DT begins to rival MT in summer frequency, as is projected to occur in an average year under END8.5 (Table 4.2), then DT+ may begin to fulfill a

similar purpose to that of MT+ at the present time, delineating the most extreme subset of DT days from the larger DT pool, possibly too large to pose a consistent risk to health. Despite its own relative increases in frequency under all three future scenarios, MT+ will likely remain infrequent enough to maintain its status as a meaningful signifier of oppressively hot and humid days that more consistently constitute a public health concern. Just as MT days on the warmer or more humid end, which fall short of qualifying as MT+, may still be associated with above-baseline mortality, the same may be true for future DT. This is especially relevant given the continued rarity of DT+ in all future scenarios, remaining much less common than MT+ even under END8.5.

On a contrary note, as DP is forecast to become increasingly rare as a potential provider of cooling relief, it is possible that other remaining synoptic types such as MP, or cooler subsets of DM and MM as MP itself decreases in frequency, might fulfill a similar role to a greater extent than they likely do already. While DP is a below-average air mass for daytime temperature, and its margin below average is likely to grow, it does not capture the coldest extremes of summer days, which most often fall under MP instead (Figure 4.9). However, likely due to its lower humidity, cooler nights, and observed reductions in summer frequency, DP is more precedented than MP in synoptic frequency and character studies as a representative of diminished summer cooling relief (Vanos et al., 2015).

Air mass character distinctions between the four simulated climate scenarios suggest that overall, the dry air mass categories can be expected to remain fairly dry until end-century, while the moist categories may become more humid sooner and, aside from MP, accrue little to no additional humidity between mid-century and end-century (Table

4.3). Under either moderate or high emissions, MT and MT+ days are not projected to increase further in daytime temperature beyond the levels reached by mid-century. Meanwhile, the bulk of their projected nighttime warming is expected to occur later in the century, especially under high emissions. This will result in a MT/MT+ diurnal temperature range that widens in mid-century and then re-narrows in end-century as nighttime warming catches up with daytime warming. Some of these results are unexpected, as narrower diurnal ranges frequently accompany increased humidity, but in this case the two effects do not show an intuitive temporal alignment. The balance of health impacts under greater humidity but only minimally warmer nights on MT/MT+ days would need to be examined specifically for Minneapolis in order to determine what this implies for mid-century public health risks. Under either end-century scenario, the combination of more humid MT/MT+ days and warmer MT/MT+ nights than under historical conditions more clearly implies a heightened risk of mortality and morbidity. The difference between moderate and high emissions is more substantial for DT days, which are expected to become hotter under MID, then either stay roughly the same under END4.5 or heat considerably further under END8.5.

Within all model-based analyses of future changes in synoptic behavior, the downscaled multi-model ensemble's inability to exactly replicate historical conditions must be taken into consideration. Aside from the frequency offsets resulting from the absence of TR days, some downscaled GCMs produced much less accurate representations of observed air mass frequency patterns over the seasonal cycle than others (Figure 4.4), and no attempt was made in this study to weigh the results of some GCMs over others. Disparities between historical model outputs and observational

records were quantified, from which the study proceeded with the assumption that the biases of each model are consistent across scenarios: an assumption in keeping with best modeling practices (Teutschbein & Seibert, 2012). Many of these disparities likely stemmed from the limitations of linear-scaling bias correction as applied by Liess et al. (2021), which only examined monthly temperature and precipitation averages rather than accounting for diurnal cycles or variability within months. Liess et al. (2021) note the possible application of alternate bias correction methods in follow-up Minnesota climate projection studies.

The availability of grid-interpolated climate normals for only temperature and precipitation, excluding other variables involved in generating SSC calendars, was likely among the greatest contributing factors to disparities in the frequency and distribution of air masses categorized from these data. In particular, the lack of bias correction for humidity helps explain several of the model-observation discrepancies noted, such as the switch in seasonal frequency peaks between DT and MT, two air mass categories for which humidity is often a greater distinguishing factor than temperature. Additionally, inherent differences exist between an observation recorded at a weather station and a simulated value representative of a model gridcell, though these are generally more consequential for precipitation, which is more highly variable at a finer spatial and temporal scale than most SSC input variables. The granularity of spatial temperature variability is critical to urban heat island studies; thermal characteristics of urban environments are known to vary at a neighborhood scale, leading to neighborhood-level disparities in health outcomes (Harlan et al., 2006). The downscaled models used in this

study are too coarse, and their representation of land cover is too limited, to capture urban-scale modifications to air mass character.

The results of this study demonstrate that the Excess Heat Factor is likely more useful as a predictor of health risk from individual events than as an indicator of long-term changes in climatology and heat wave recurrence. Its dependence on location-specific climatological thresholds renders it a relative rather than absolute metric, which is exactly what drives its usefulness in health studies. Other studies (Habeeb et al., 2015; Meehl & Tebaldi, 2004) have identified more prominent upward historical trends in heat wave duration and frequency in other Midwestern locations, though mostly further south than Minnesota, using other heat wave definitions. This study is not intended to compare the relative usefulness of different heat wave metrics, instead merely focusing on one with an increasingly proven record of meaningfully relating to health outcomes. A further examination could potentially indicate whether heat wave trends in Minnesota appear more clearly under the usage of other criteria, especially those involving apparent temperature.

Chapter 6: Conclusion

The findings of this study demonstrate that while some changes in the behavior of extreme heat conditions in Minnesota are already occurring, much more drastic changes can be expected in the remainder of the 21st century. Some changes, such as the increasing frequency of MT at the expense of DP, and the overall pattern of nighttime warming, have already been observed and are projected to continue. Other expected changes, especially the increased frequency and temperature of DT days, represent new directions in Minnesota's climate not foreshadowed by the previous seven decades. Some warming trends within air mass types are projected to continue throughout the century, to varying degrees by end-century depending on greenhouse gas emissions, while others may reach their full extent by mid-century and change minimally from there. Overall, nighttime warming trends are expected to continue late in the century even after some daytime warming trends have slowed. While the health risks associated with each of these changes must be evaluated individually in order to accurately predict future mortality, as a whole they indicate a future in which Minnesotans face a considerably more severe threat.

While this study's analyses of climate projections focused more narrowly on Minneapolis, the findings reflect a more widespread warming trend that applies to other locations across the region. However, Minnesota does not experience heat events evenly across all regions within the state, and overall warming is expected to show the greatest magnitude in northern Minnesota (Liess et al., 2021). Further studies could extend these analyses across other urban locations such as Rochester, Duluth, and Fargo-Moorhead, in order to highlight unique features of the extreme heat conditions each one may expect throughout this century.

Regardless of the magnitude of the heat-related risk facing each location, Minnesota's urban population centers will need to be prepared to address the health concerns associated with the growing frequency, duration, and intensity of extreme heat events. Such preparations will need to draw from a thorough understanding of the unique sensitivities of each city population's health responses to heat. This can be accomplished through predictive algorithms (Hayhoe et al., 2010; Sheridan & Kalkstein, 2004) or other relative risk-based assessments (Curriero et al., 2002; Kalkstein et al., 2018), which can then be applied to future climate projections for an urban location (Sheridan et al., 2012). A critical component of local heat-health evaluations is the identification and quantification of disparities in health outcomes based on age, race, income, and other demographics. This can then facilitate more targeted "cool cities solutions" efforts toward specific neighborhoods or populations where vulnerabilities are greatest (de Guzman et al., 2020).

Amidst a variety of growing climate threats, it is important to remember that heat-related deaths and illnesses are preventable through increased precautions at both the individual and community level (Luber & McGeehin, 2008). Heat-health warning systems have demonstrated effectiveness in reducing mortality when tailored to locally specific meteorological criteria known to display stronger relationships with health responses (Sheridan & Kalkstein, 2004). The development of more location-specific predictive algorithms for mortality during heat events could assist Minneapolis and other urban communities in Minnesota in issuing warnings when they are most needed, rather than using heat index thresholds more broadly applied across a larger region. The results

of this study may hopefully provide important and helpful groundwork toward building greater resilience within Minnesota's cities in the face of extreme heat.

Tables

Model	Institution	Resolution (°)	Reference
bcc-csm1-1	BCC (China)	1 x 1.33	(Wu et al., 2010)
CCSM4	NCAR (USA)	0.9 x 1.25	(Gent et al., 2011)
CMCC-CM	CMCC (Italy)	0.75 x 0.75	(Scoccimarro et al., 2011)
CNRM-CM5	CNRM-CERFACS (France)	1.5 x 1.5	(Voldoire et al., 2013)
GFDL-ESM2M	NOAA-GFDL (USA)	2 x 2.5	(Dunne et al., 2012)
IPSL-CM5A-LR	IPSL (France)	1.875 x 3.75	(Dufresne & Bony, 2008)
MIROC5	MIROC (Japan)	2.8 x 2.8	(Watanabe et al., 2010)
MRI-CGCM3	MRI (Japan)	1.125 x 1.125	(Yukimoto et al., 2012)

Table 2.1: List of GCMs for boundary conditions, from Liess et al. (2021).

		All			DP			DT			MT			MT+		
		Mean	Slope	R ²	Mean	Slope	R ²	Mean	Slope	R ²	Mean	Slope	R ²	Mean	Slope	R ²
Minneapolis	Frequency	-	-	-	11.1	-1.079	0.134	6	0.164	0.003	26.1	1.691	0.163	2	0.152	0.023
	3:00 T _a	17.3	0.297	0.270	12.1	0.178	0.065	20.1	0.12	0.01	20	0.167	0.144	24.3	0.085	0.012
	3:00 T _d	13.6	0.184	0.121	8.5	0.046	0.004	14.1	-0.005	0	16.9	0.099	0.060	18.9	0.117	0.016
	15:00 T _a	25.4	0.055	0.009	21.2	-0.043	0.007	32.3	-0.195	0.048	28.2	-0.046	0.017	33.1	-0.073	0.013
	15:00 T _d	13.8	0.097	0.03	8	-0.097	0.015	13.7	-0.392	0.055	18.1	-0.023	0.002	19.9	-0.117	0.018
Rochester	Frequency	-	-	-	13.5	-0.01	0	4.6	-0.529	0.035	27	1.801	0.152	1	0.061	0.007
	3:00 T _a	15.6	0.143	0.092	10.6	0.192	0.112	17.8	-0.054	0.002	18.8	0.013	0.001	23.4	-0.053	0.006
	3:00 T _d	13.2	0.211	0.145	8.3	0.173	0.070	13.1	-0.175	0.011	16.8	0.106	0.065	19.7	0.077	0.009
	15:00 T _a	24.4	-0.082	0.02	20.7	-0.016	0.001	31.2	-0.102	0.012	27.4	-0.139	0.141	32.6	-0.08	0.014
	15:00 T _d	14.6	0.257	0.179	9.2	0.282	0.116	13.7	-0.413	0.061	18.9	0.14	0.100	20.9	0.013	0
Duluth	Frequency	-	-	-	19.8	-1.128	0.109	2.2	-0.017	0	12.8	1.188	0.145	0.3	0.021	0.005
	3:00 T _a	12.8	0.259	0.250	8.5	0.223	0.187	15.9	-0.119	0.008	17.5	0.081	0.022	21.4	-0.269	0.068
	3:00 T _d	10.2	0.196	0.124	6	0.141	0.050	10.6	-0.027	0	15.2	0.109	0.031	16.7	-0.278	0.044
	15:00 T _a	21.2	0.161	0.079	18.5	-0.004	0	29.4	-0.148	0.023	26.6	-0.17	0.092	30.5	-0.195	0.042
	15:00 T _d	11.5	0.166	0.096	7	0.086	0.016	11.3	-0.089	0.002	17.2	-0.087	0.02	18.1	-0.328	0.04
Fargo	Frequency	-	-	-	16.9	-0.389	0.021	6	-0.331	0.015	21.1	1.034	0.086	1	0.088	0.018
	3:00 T _a	15.2	0.203	0.179	10.3	0.222	0.181	18.2	0.094	0.008	18.8	0.108*	0.063*	23.2	0.118	0.018
	3:00 T _d	12.1	0.172	0.114	8	0.157	0.068	12.5	-0.048	0.001	16.1	0.077	0.022	18.6	0.321	0.061
	15:00 T _a	25	0.042	0.005	21.4	0.108*	0.046*	32.5	-0.132	0.027	28	-0.143	0.106	33.3	-0.07	0.005
	15:00 T _d	12.7	0.164	0.090	8.1	0.17	0.055	12.7	-0.035	0.001	17.6	0.031	0.003	19.9	-0.149	0.017

Table 3.1: Summary statistics for urban sites' air mass frequency (days per season), air temperature (T_a; °C), and dew point temperature (T_d; °C) trends over 1948-2019 within the May 20-September 10 season. Linear regression slopes are expressed as decadal rather than yearly changes. Bold slope and R² values indicate p < 0.05 significance.

*Fargo's daily maximum DP temperatures increased with p < 0.05 significance, while DP temperatures at 15:00 did not. Conversely, Fargo's MT temperatures at 3:00 increased with p < 0.05 significance, while daily minimum MT temperatures did not. Statistical significance between daily and hourly datasets matched for all other trends.

	All			DP			DT			MT			MT+		
	Mean	Slope	R ²	Mean	Slope	R ²	Mean	Slope	R ²	Mean	Slope	R ²	Mean	Slope	R ²
Minneapolis	11.1	-0.239	0.355	11.5	-0.255	0.156	14.2	-0.221	0.083	10.8	-0.206	0.367	11.2	-0.054	0.005
Jordan	12.5	-0.156	0.037	13.2	-0.29	0.077	15.3	-0.116	0.011	11.8	-0.108	0.025	11.9	0.002	0
Rochester	11.7	-0.288	0.352	12.5	-0.279	0.267	15.4	-0.041	0.003	11.2	-0.214	0.427	11.6	-0.061	0.014
Grand Meadow	11.9	-0.091	0.043	12.4	-0.194	0.094	13.8	0.085	0.009	11.3	0.008	0	11.9	-0.102	0.021
Duluth	11.7	-0.134	0.129	12.7	-0.244	0.242	15.8	-0.085	0.01	12.2	-0.301	0.308	12	-0.077	0.004
Two Harbors	11.4	-0.274	0.409	11.6	-0.243	0.207	16.1	-1.033	0.343	11.7	-0.606	0.350	13.9	-0.299	0.017
Fargo	13	-0.149	0.121	13.9	-0.063	0.018	16.7	-0.21	0.071	12.2	-0.193	0.231	13.4	-0.315	0.085
Ada	13.8	-0.28	0.248	14.3	-0.361	0.288	16.7	-0.418	0.193	13	-0.146	0.075	14.4	-0.34	0.076

Table 3.2: Summary statistics for paired urban and rural sites' trends in diurnal temperature range (°C) over 1948-2019 within the May 20-September 10 season. Linear regression slopes are expressed as decadal rather than yearly changes. Bold slope and R² values indicate p < 0.05 significance.

	Minneapolis			Rochester			Duluth			Fargo		
	Mean	Slope	R ²	Mean	Slope	R ²	Mean	Slope	R ²	Mean	Slope	R ²
Consecutive run frequency	0.8	0.027	0.002	0.4	0.013	0.001	0.2	0.001	0	0.7	-0.014	0.001
Consecutive run duration	4.2	0.221	0.128	4.2	-0.32	0.245	3.3	-0.117	0.143	3.6	-0.085	0.027

Table 3.3: Summary statistics for urban sites' trends in frequency (occurrences per summer) and duration (days per occurrence) of consecutive runs of 3 or more MT+/DT days over 1948-2019 within the May 20-September 10 season. Linear regression slopes are expressed as decadal rather than yearly changes. Bold slope and R² values indicate $p < 0.05$ significance.

	Minneapolis			Rochester			Duluth			Fargo		
T ₉₅	25.8			24.2			21.7			24.7		
EHF ₈₅	17.8			15.7			17.4			18.1		
	Mean	Slope	R ²	Mean	Slope	R ²	Mean	Slope	R ²	Mean	Slope	R ²
Heat wave frequency	3.5	0.154	0.025	3.9	-0.063	0.004	3.7	0.132	0.019	4	-0.028	0.001
Heat wave duration, annual mean	5.8	-0.073	0.007	5.5	-0.14	0.032	5.4	0.074	0.009	5	-0.007	0
Heat wave duration, annual maximum	8.6	0.096	0.002	8.9	-0.37	0.027	7.8	0.423	0.062	7.5	-0.003	0
Heat wave season length	52.9	2.225	0.02	61.3	-0.773	0.002	48.8	2.948	0.044	56.4	1.407	0.011
Heat wave season starting date	174.2	-0.622	0.004	169.5	0.664	0.004	179.6	-1.244	0.016	176.4	-0.032	0
Exceedance of T ₉₅ on heat wave days	0.8	-0.029	0.016	0.8	-0.038	0.028	0.8	0.039	0.03	0.8	-0.037	0.031
Exceedance T ₉₅ on severe heat wave days	3.1	0.062	0.04	2.9	0.003	0	3.3	0.052	0.033	3.1	-0.013	0.001
Number of heat wave days	20.8	0.884	0.018	22	-0.896	0.02	19.9	1.316	0.049	20.7	0.037	0
Number of severe heat wave days	3.8	-0.083	0.002	4	-0.296	0.016	3.7	0.021	0	3.5	-0.225	0.016

Table 3.4: Summary statistics for urban sites' trends in positive-EHF heat wave events over 1948-2019. T₉₅ indicates the 95th-percentile temperature threshold (°C), while EHF₈₅ indicates the 85th-percentile EHF value threshold (°C²). Frequency and duration are expressed as in Table 3.3. Heat wave season starting dates are expressed as Julian dates. Linear regression slopes are expressed as decadal rather than yearly changes. Bold slope and R² values indicate p < 0.05 significance.

		DP	DM	DT	MP	MM	MT	MT+	TR
Minneapolis	All heat wave days	0	274	299	1	35	642	139	161
		(0.0%)	(17.7%)	(19.3%)	(0.1%)	(2.3%)	(41.4%)	(9.0%)	(10.4%)
	Severe heat wave days	0	16	105	0	0	70	73	24
		(0.0%)	(5.6%)	(36.5%)	(0.0%)	(0.0%)	(24.3%)	(25.3%)	(8.3%)
Rochester	All heat wave days	1	310	229	0	67	786	73	139
		(0.1%)	(19.3%)	(14.3%)	(0.0%)	(4.2%)	(49.0%)	(4.5%)	(8.7%)
	Severe heat wave days	0	15	88	0	1	110	46	29
		(0.0%)	(5.2%)	(30.4%)	(0.0%)	(0.3%)	(38.1%)	(15.9%)	(10.0%)
Duluth	All heat wave days	12	501	109	4	148	554	25	110
		(0.8%)	(34.2%)	(7.5%)	(0.3%)	(10.1%)	(37.9%)	(1.7%)	(7.5%)
	Severe heat wave days	1	56	45	0	5	130	17	16
		(0.4%)	(20.7%)	(16.7%)	(0.0%)	(1.9%)	(48.1%)	(6.3%)	(5.9%)
Fargo	All heat wave days	5	376	302	1	35	558	70	156
		(0.3%)	(25.0%)	(20.1%)	(0.1%)	(2.3%)	(37.1%)	(4.7%)	(10.4%)
	Severe heat wave days	0	22	97	0	1	70	42	22
		(0.0%)	(8.7%)	(38.2%)	(0.0%)	(0.4%)	(27.6%)	(16.5%)	(8.7%)

Table 3.5: Allocation of daily SSC categories within all positive-EHF heat wave days and within severe heat wave days only. Values are expressed as total days over 1948-2019 and as percentages of each location's heat wave or severe heat wave days.

		Observed mean	Simulated mean	Mean bias error	RMSD	Percent error
3:00 temperature	June	16.4	17.1	0.71	1.85	4.36
	July	19.0	19.5	0.47	1.54	2.49
	August	17.9	18.7	0.82	1.85	4.57
3:00 dew point	June	12.4	12.0	-0.47	1.97	-3.75
	July	15.6	14.0	-1.61	2.10	-10.26
	August	15.0	13.2	-1.80	2.36	-12.01
15:00 temperature	June	24.7	24.4	-0.35	1.99	-1.43
	July	27.2	27.6	0.40	2.12	1.47
	August	25.7	26.3	0.56	1.95	2.18
15:00 dew point	June	13.0	13.1	0.20	2.10	1.51
	July	15.7	15.0	-0.72	1.79	-4.58
	August	15.5	14.1	-1.43	2.27	-9.20
Air mass frequency	DM	32.0	40.9	8.93	11.31	27.91
	DP	12.6	5.3	-7.33	9.77	-58.13
	DT	4.7	13.0	8.35	11.54	179.57
	MM	19.6	22.2	2.65	7.33	13.55
	MP	4.6	11.2	6.61	7.09	143.61
	MT	27.0	20.4	-6.53	11.70	-24.21
	MT+	1.7	1.0	-0.69	1.68	-41.67

Table 4.1: Historical multi-model ensemble agreement with JJA monthly temperature averages (°C) and air mass frequency (days per May 20-September 10 season) in Minneapolis weather station observations. All rows represent 20 observations, with one value per year from 1980 to 1999, as shown in Figures 4.6-4.7.

		HIST		MID		END4.5		END8.5	
		Mean	Std Dev	Mean	Std Dev	Mean	Std Dev	Mean	Std Dev
Air mass frequency	DP	5.3	5.7	3.8	3.8	2.5	2.3	1.2	1.6
	DM	40.9	14.2	40.7	12.8	34.5	11.6	28.7	10.6
	DT	13.0	12.8	17.6	14.1	21.0	16.0	26.9	20.4
	MP	11.2	7.3	7.2	5.7	7.5	5.0	5.9	4.6
	MM	22.2	16.5	14.8	8.7	18.5	13.5	16.5	11.1
	MT	20.4	9.2	27.7	11.6	26.4	11.0	29.5	11.5
	MT+	1.0	1.3	2.2	2.5	3.5	3.5	5.3	4.6
Consecutive runs	Frequency	1.8	1.9	2.6	2.2	3.1	2.2	3.9	2.4
	Duration	5.3	3.3	5.3	3.3	5.8	4.1	6.5	5.4

Table 4.2: Summary statistics for simulated air mass frequency (days per season), as well as frequency (occurrences per season) and duration (days per occurrence) of consecutive runs of 3 or more MT+/DT days. All statistics represent Minneapolis within the May 20-September 10 season over four climate scenarios. Air mass frequencies and consecutive run frequencies represent 160 observations, with one value per model-year combination. Consecutive run durations represent individual events unaggregated by model or year (number of observations = $160 \times$ number of events per average model-year). Bold mean values indicate significant changes from HIST ($p < 0.05$ by t-test).

		HIST		MID		END4.5		END8.5	
		Mean	Std Dev	Mean	Std Dev	Mean	Std Dev	Mean	Std Dev
3:00 temperature	All	18.0	4.5	19.0	4.7	21.1	4.4	23.0	4.3
	DP	11.1	3.5	11.3	3.3	13.9	4.0	14.8	3.2
	DM	17.8	3.9	17.9	4.4	20.4	3.9	22.0	3.7
	DT	21.2	3.3	22.8	3.5	24.1	3.2	26.0	3.0
	MP	12.7	3.5	13.3	3.3	14.2	3.4	15.5	3.1
	MM	18.6	3.2	18.6	3.4	19.9	3.3	20.8	3.4
	MT	20.1	3.3	20.6	3.2	22.3	3.4	23.5	3.4
	MT+	23.9	2.7	24.4	2.6	26.2	2.3	27.0	2.6
3:00 dew point	All	12.8	4.0	14.0	4.1	14.2	3.7	15.6	3.8
	DP	8.4	3.8	8.8	3.3	10.0	4.1	10.4	3.7
	DM	11.8	3.7	12.5	3.7	13.0	3.5	14.2	3.6
	DT	12.6	3.9	13.3	3.9	13.5	3.5	15.1	3.7
	MP	10.0	3.7	10.8	3.6	11.3	3.7	12.4	3.5
	MM	14.2	3.1	15.0	3.2	15.4	3.2	16.1	3.5
	MT	15.8	2.9	17.1	2.9	16.5	2.6	17.6	2.8
	MT+	17.5	3.6	18.8	3.4	17.0	2.8	18.4	3.1
15:00 temperature	All	25.3	6.4	28.2	6.5	27.8	6.4	29.8	6.9
	DP	22.8	3.8	23.4	3.8	24.5	4.4	24.4	3.9
	DM	27.7	4.2	29.5	4.6	29.5	4.7	30.8	5.0
	DT	33.7	3.7	35.2	4.1	35.1	3.9	37.3	4.5
	MP	15.1	3.7	16.3	3.8	16.7	3.7	18.2	3.6
	MM	20.5	3.3	21.6	3.5	21.7	3.1	22.2	3.2
	MT	26.5	3.9	28.7	4.2	27.3	3.5	28.3	3.7
	MT+	29.6	3.4	32.2	4.5	30.4	2.7	31.6	3.3
15:00 dew point	All	13.8	4.3	15.3	4.7	15.2	3.9	16.5	3.9
	DP	10.5	4.8	10.5	4.3	12.3	4.4	12.4	4.0
	DM	12.8	3.7	13.7	4.0	14.1	3.4	15.2	3.4
	DT	12.6	3.8	13.6	3.8	13.6	3.3	15.2	3.4
	MP	10.5	3.5	11.3	3.4	11.7	3.5	13.0	3.5
	MM	15.0	3.2	16.1	3.4	16.1	3.2	16.7	3.3
	MT	17.7	3.7	19.4	3.6	18.1	3.0	19.1	3.2
	MT+	19.3	4.4	20.7	3.9	18.2	3.4	19.8	3.7
Diurnal temperature range	All	7.3	5.9	9.2	5.9	6.8	5.5	6.8	5.6
	DP	11.6	4.2	12.1	3.9	10.6	4.7	9.6	4.4
	DM	9.9	5.0	11.5	5.0	9.0	4.7	8.8	4.7
	DT	12.5	4.8	12.5	5.4	11.0	5.2	11.3	5.2
	MP	2.4	3.6	3.0	3.6	2.6	3.4	2.7	3.3
	MM	1.9	3.4	3.0	3.9	1.8	3.2	1.4	2.9
	MT	6.4	4.7	8.2	4.9	5.0	4.1	4.8	4.3
	MT+	5.7	4.3	7.8	5.5	4.2	3.1	4.6	3.9

Table 4.3: Summary statistics for simulated Minneapolis air mass temperatures (°C) within May 20-September 10 over four climate scenarios. All rows summarize individual days unaggregated by model or year (number of observations = 160 × days per average model-year). Bold mean values indicate significant changes from HIST ($p < 0.05$ by t-test).

		HIST		MID		END4.5		END8.5	
		Mean	Std Dev	Mean	Std Dev	Mean	Std Dev	Mean	Std Dev
T ₉₅		26.3	1.1	28.2	1.5	29.0	1.3	30.9	2.2
EHF ₈₅	From HIST T ₉₅	13.2	5.0	19.9	4.3	18.3	3.0	23.6	7.4
	From own T ₉₅	13.2	5.0	16.3	5.1	11.6	3.0	11.5	2.7
Heat wave frequency	From HIST T ₉₅	3.3	1.9	5.4	1.9	5.4	1.9	6.0	2.1
	From own T ₉₅	3.3	1.9	3.5	1.7	3.1	1.6	3.0	1.5
Heat wave duration	From HIST T ₉₅	6.6	5.1	7.4	6.2	9.2	8.9	11.6	11.5
	From own T ₉₅	6.6	5.1	6.1	4.1	6.9	5.5	7.0	5.8
Heat wave season length	From HIST T ₉₅	47.2	29.3	84.0	30.7	90.5	28.1	111.7	30.3
	From own T ₉₅	47.2	29.3	51.5	28.7	45.1	28.7	42.3	27.5
Heat wave season starting date	From HIST T ₉₅	178.2	20.6	161.1	23.0	155.4	22.2	143.0	22.5
	From own T ₉₅	178.2	20.6	176.5	23.1	176.7	20.8	178.7	18.7
Exceedance of T ₉₅ on heat wave days	From HIST T ₉₅	0.9	1.8	1.4	2.6	1.7	2.3	2.3	3.0
	From own T ₉₅	0.9	1.8	1.0	2.0	0.9	1.6	0.9	1.6
Exceedance of T ₉₅ on severe heat wave days	From HIST T ₉₅	2.8	1.8	4.4	2.1	4.0	1.6	5.2	2.5
	From own T ₉₅	2.8	1.8	3.1	1.7	2.6	1.4	2.5	1.4
Number of heat wave days	From HIST T ₉₅	21.6	15.3	47.4	24.1	58.6	25.0	82.4	28.6
	From own T ₉₅	21.6	15.3	21.4	11.1	21.3	13.9	21.1	13.6
Number of severe heat wave days	From HIST T ₉₅	3.8	4.9	8.9	7.0	11.3	7.8	16.3	8.8
	From own T ₉₅	3.8	4.9	3.8	4.2	3.9	4.4	4.0	4.0

Table 4.4: Summary statistics for simulated trends in positive-EHF heat wave events, defined either from each model’s HIST T₉₅ threshold and applied across all scenarios within that model (“no acclimatization”), or from each model-scenario combination’s own T₉₅ threshold (“full acclimatization”). All statistics represent Minneapolis within the May 20-September 10 season over four climate scenarios. T₉₅ indicates the 95th-percentile temperature threshold (°C), while EHF₈₅ indicates the 85th-percentile EHF value threshold (°C²); means and standard deviations for these summarize eight values, one from each model-scenario. Heat wave frequencies, heat wave season lengths, heat wave season starting dates (Julian date), number of heat wave days, and number of severe heat waves represent 160 observations, with one value per model-year combination. All other rows represent individual days or events unaggregated by model or year (number of observations = 160 × number of days or events per average model-year). Bold mean values indicate significant changes from HIST (p < 0.05 by t-test).

Figures



Figure 2.1: Locations of weather stations from which historical temperature records were used. Larger markers labeled in bold represent urban airport stations.

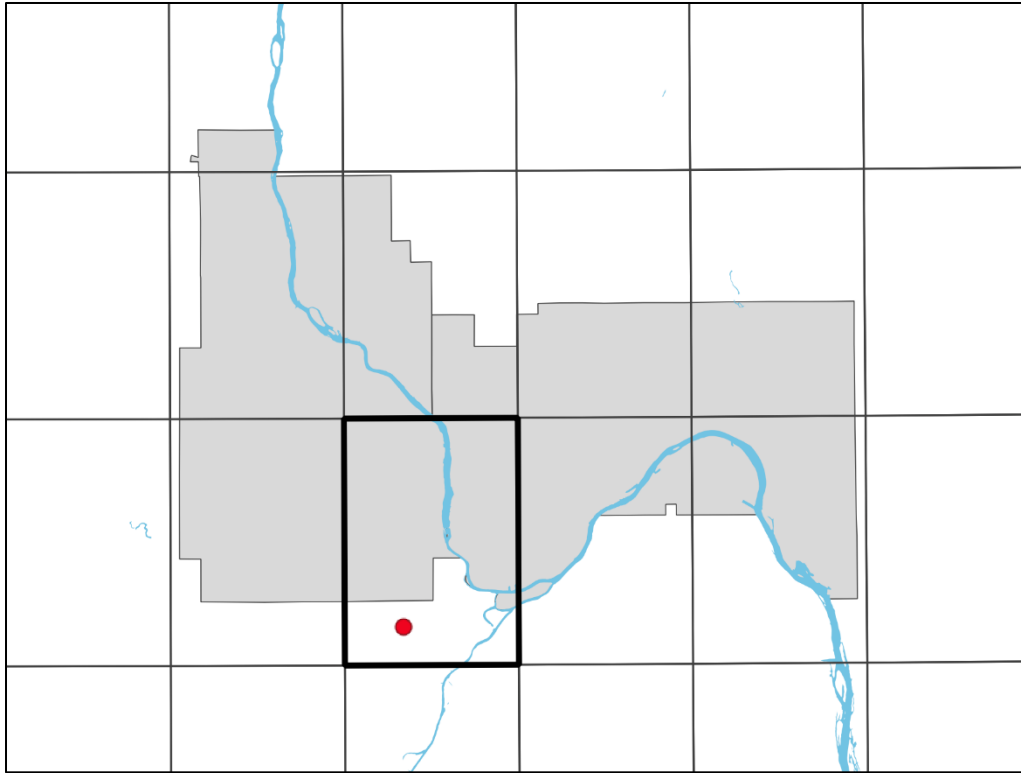


Figure 2.2: The scale of the downscaled model grid over Minneapolis and St. Paul, Minnesota. The location of the Minneapolis airport is marked, and the bolded gridcell that includes it provided the data used in this analysis.

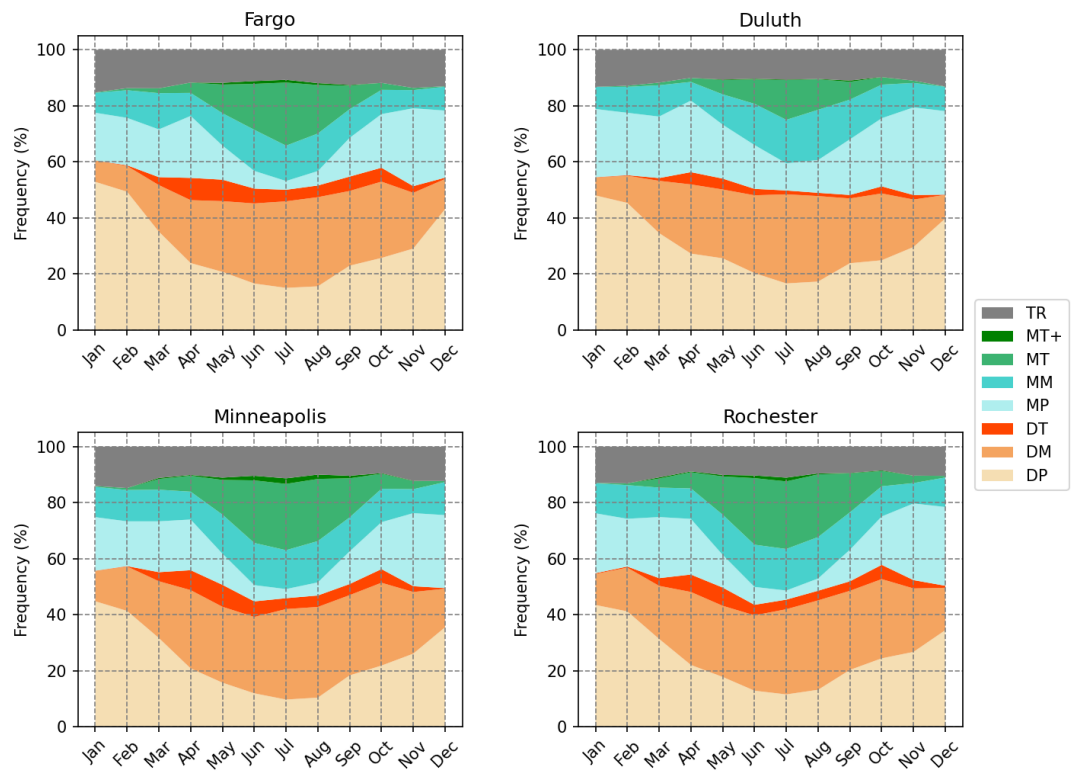


Figure 3.1: Monthly frequency (percent of total days in each month) of air mass types by location, averaged over 1948-2019.

Minneapolis - Historical runs, 1980-1999

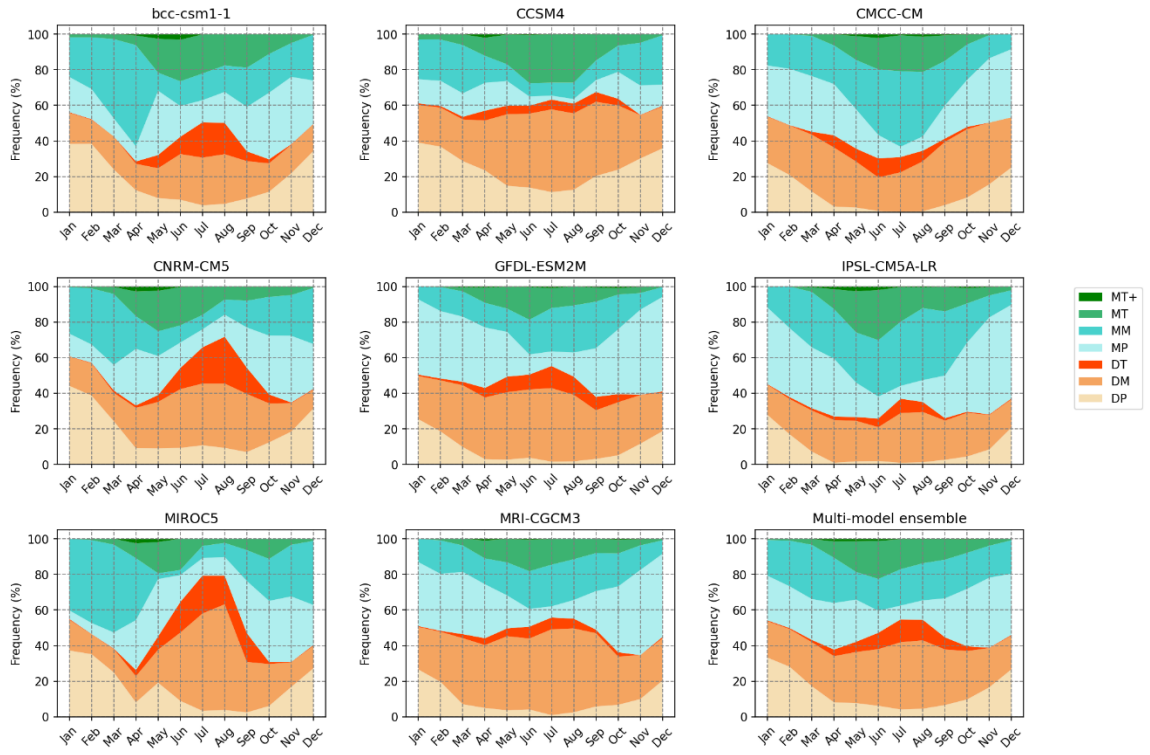


Figure 4.1: Average monthly frequency distributions of air mass categories in the multi-model ensemble under the historical scenario (HIST; 1980-1999).

Minneapolis - RCP4.5, 2040-2059

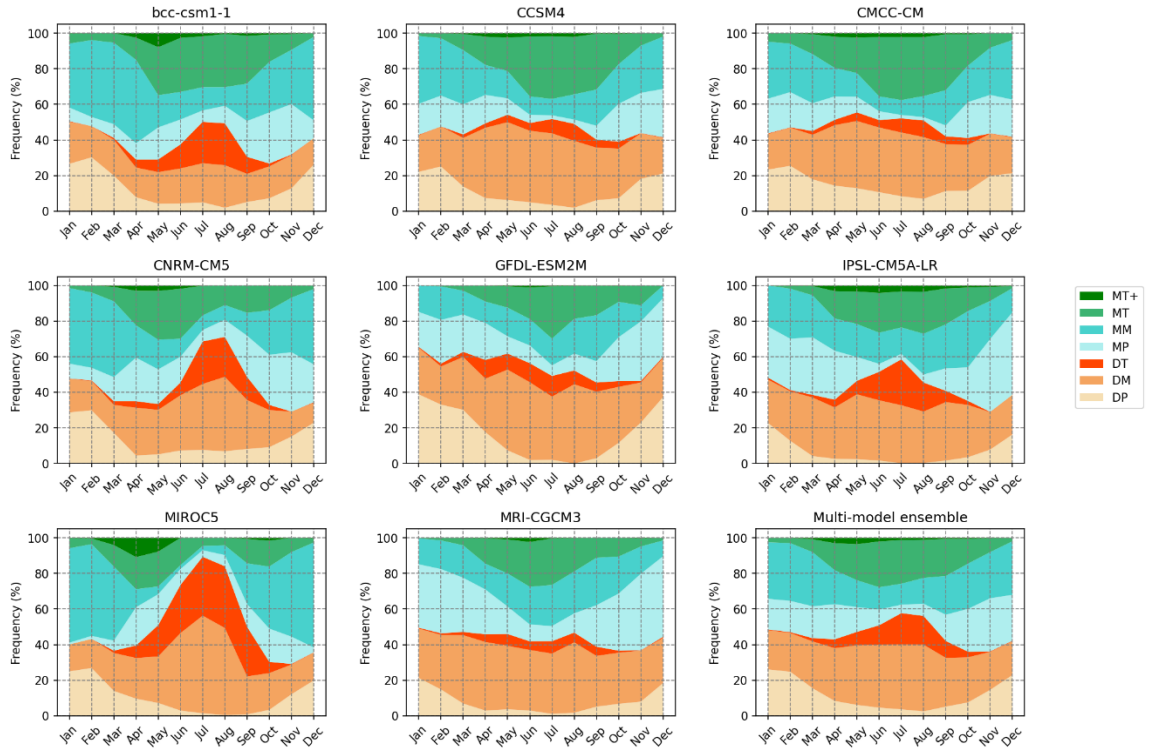


Figure 4.2: As Figure 4.1, but under the mid-century scenario (MID; 2040-2059).

Minneapolis - RCP4.5, 2080-2099

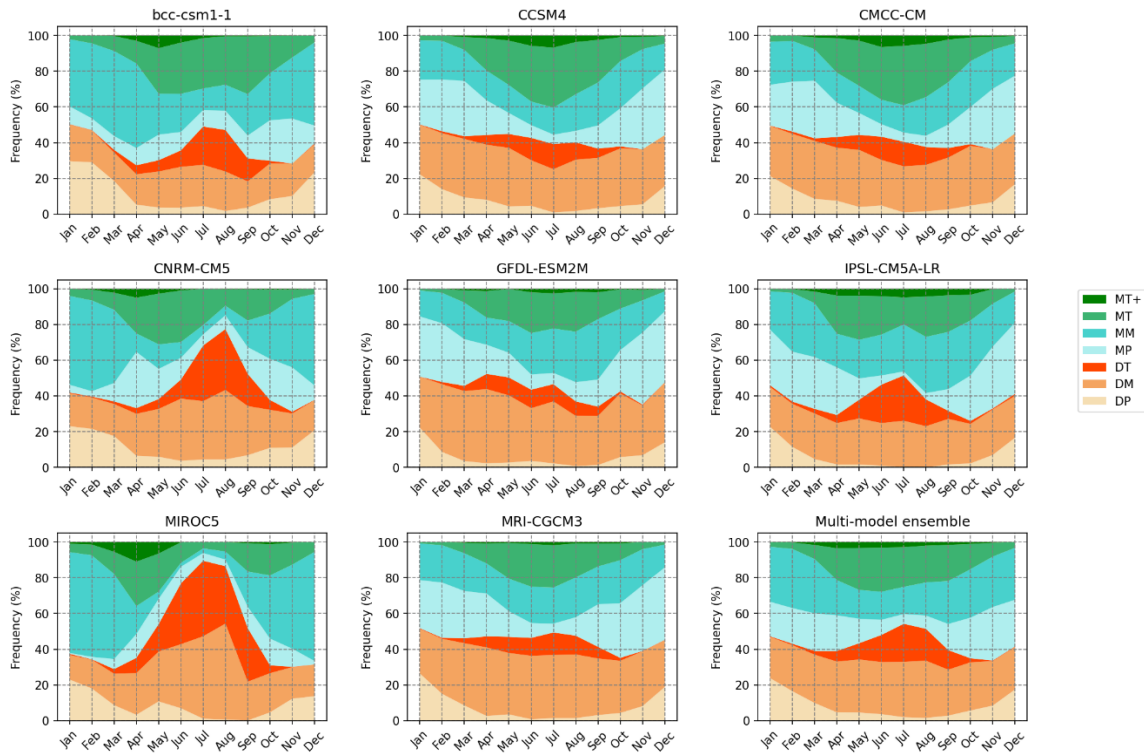


Figure 4.3: As Figure 4.1, but under the late-century moderate-emissions scenario (END4.5; 2080-2099).

Minneapolis - RCP8.5, 2080-2099

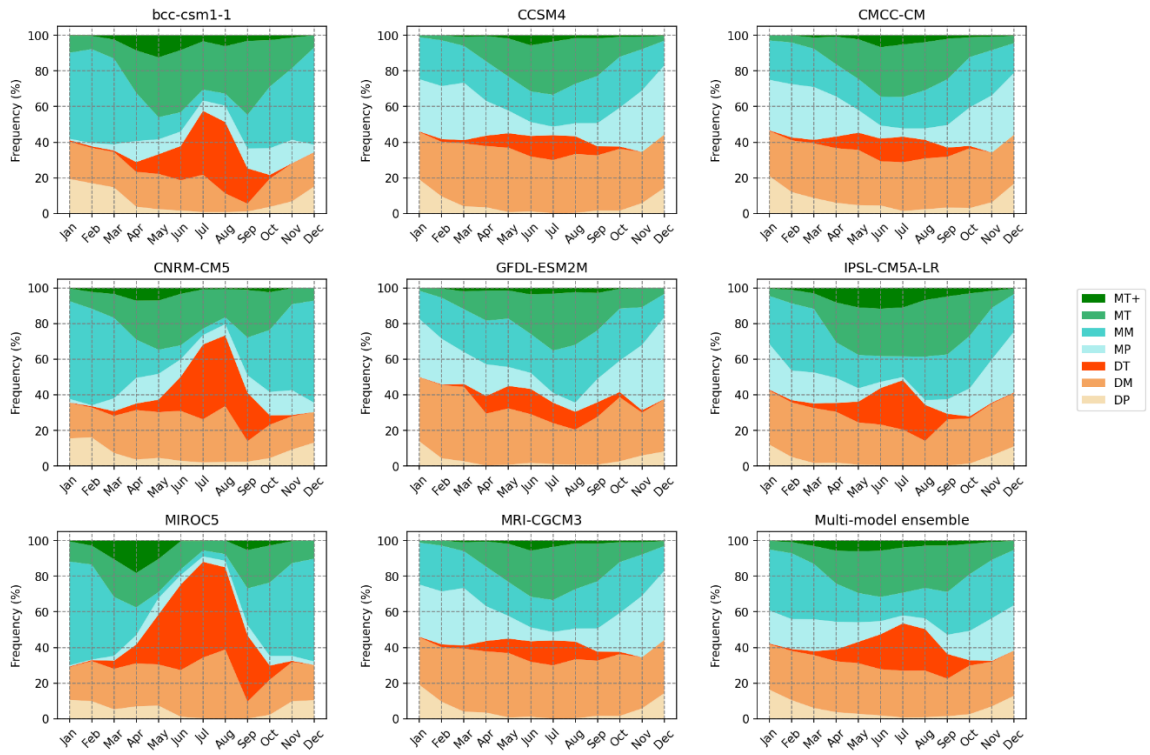


Figure 4.4: As Figure 4.1, but under the late-century high-emissions scenario (END8.5; 2080-2099).

Minneapolis air mass frequency

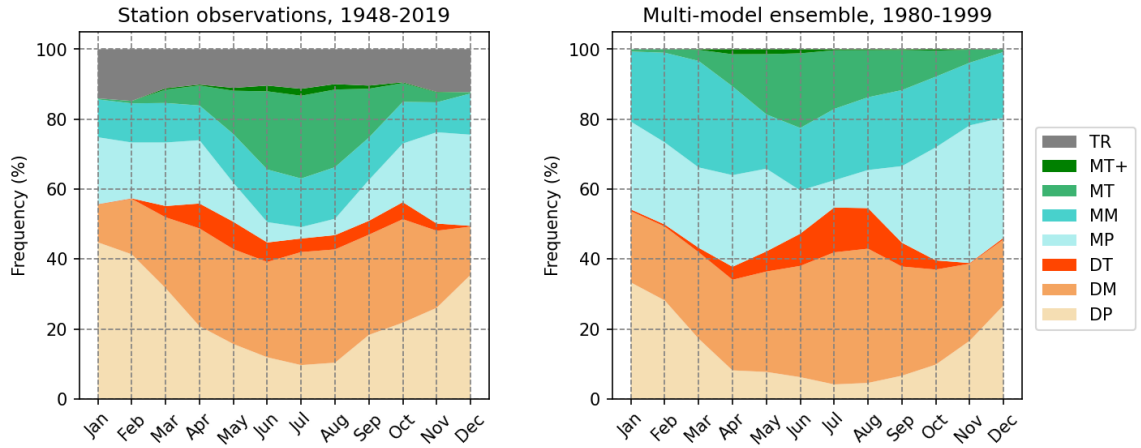


Figure 4.5: Average monthly frequency distributions of air mass categories in Minneapolis station observations (1948-2019) and the multi-model ensemble (1980-1999). The TR (Transition) category occurs in the historical record but was not assigned for model outputs.

Model-observation agreement, Minneapolis 1980-1999

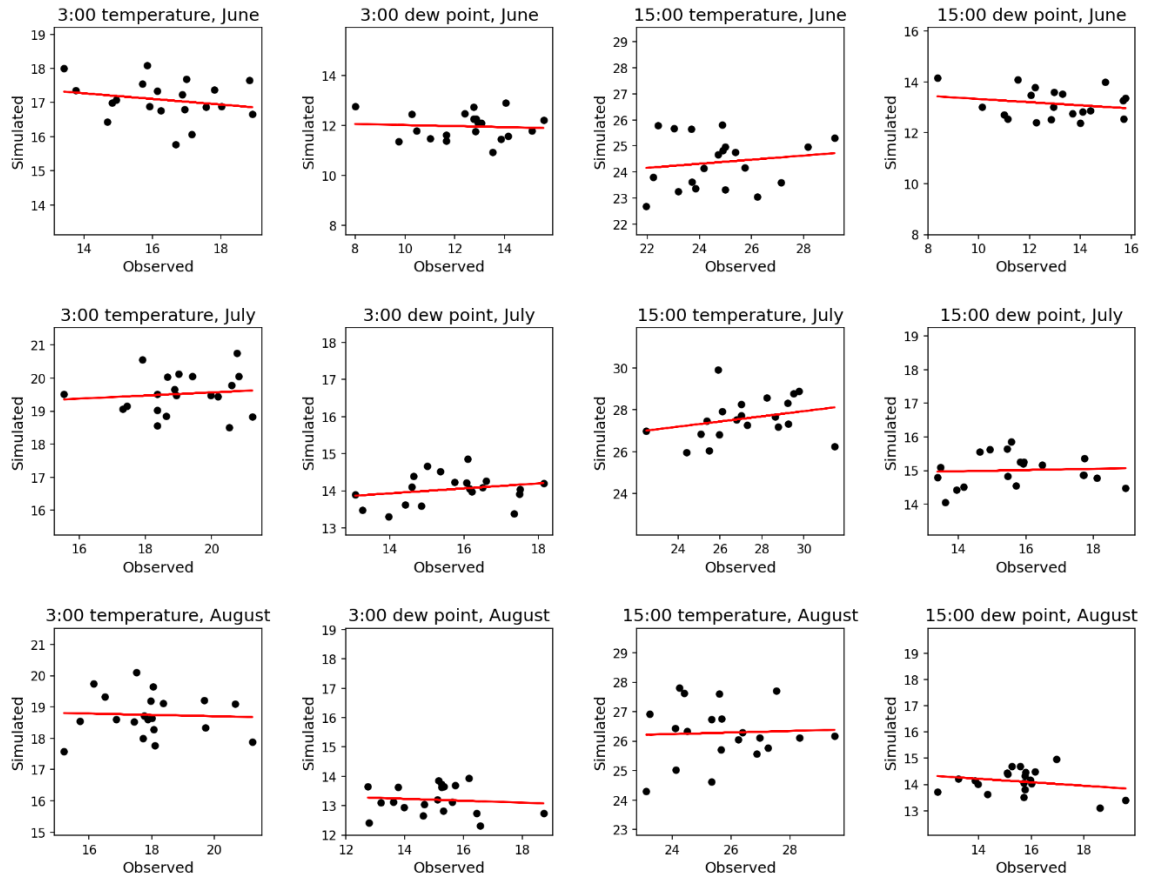


Figure 4.6: Historical multi-model ensemble agreement with JJA monthly temperature averages ($^{\circ}\text{C}$) in Minneapolis weather station observations in 1980-1999. X-axis and y-axis scales correspond within each plot but not between plots.

Model-observation agreement, Minneapolis 1980-1999

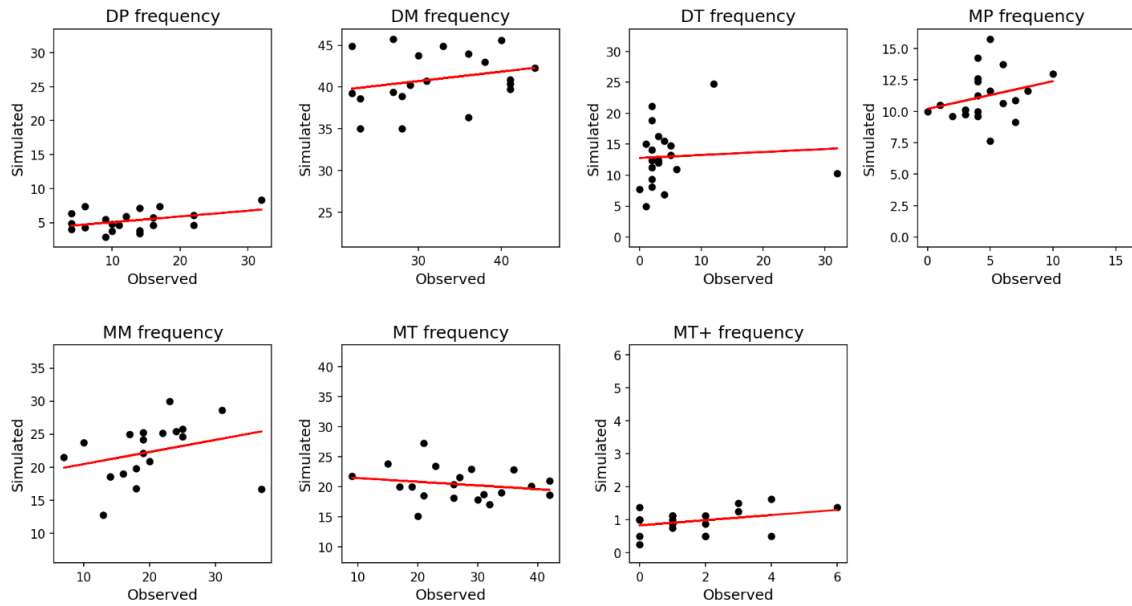


Figure 4.7: Historical multi-model ensemble agreement with air mass frequency (days per May 20-September 10 season) in Minneapolis weather station observations in 1980-1999. X-axis and y-axis scales correspond within each plot but not between plots.

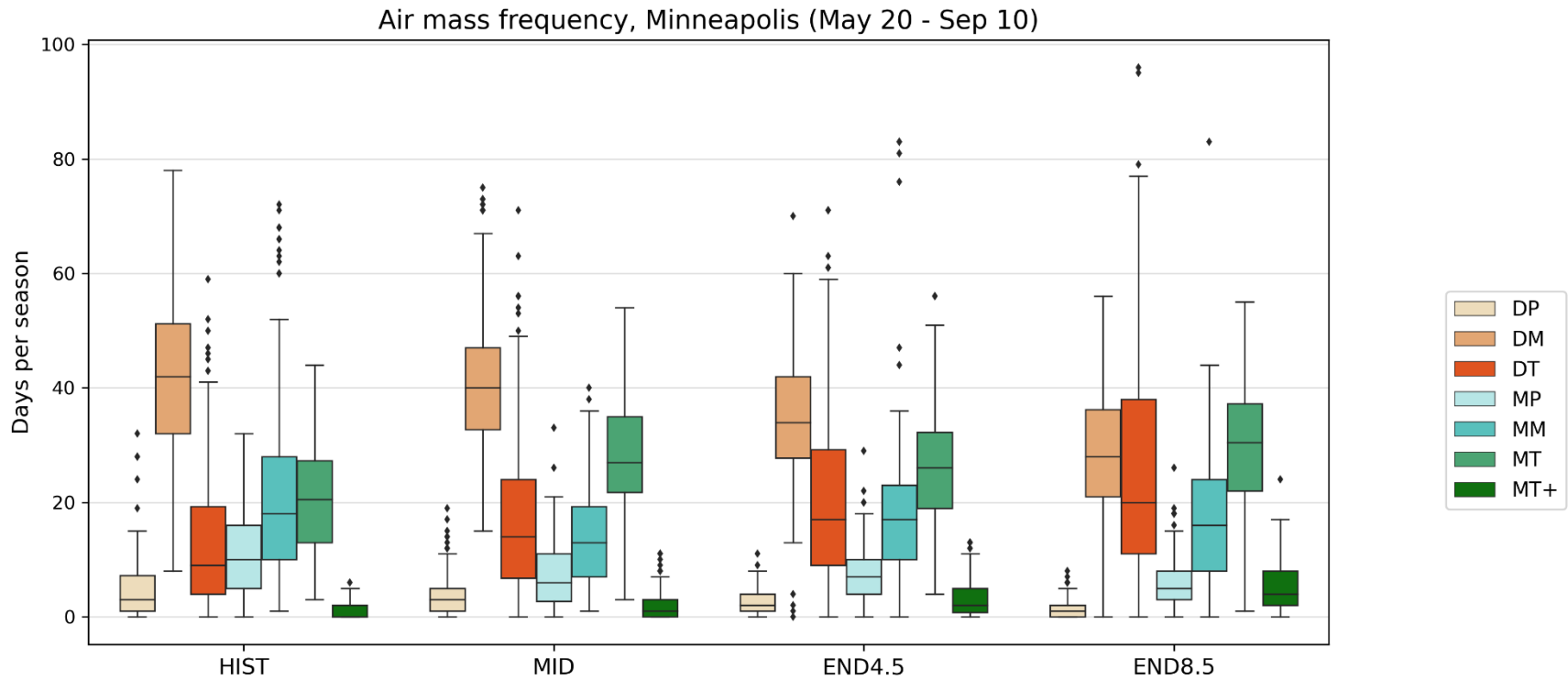


Figure 4.8: Distributions of summer (May 20-September 10) air mass frequency by scenario. Whiskers indicate $1.5 \times \text{IQR}$, with outlying values plotted individually, as also applicable to Figures 4.9-4.23. Each observation represents one model-year combination (see Table 4.2 description).

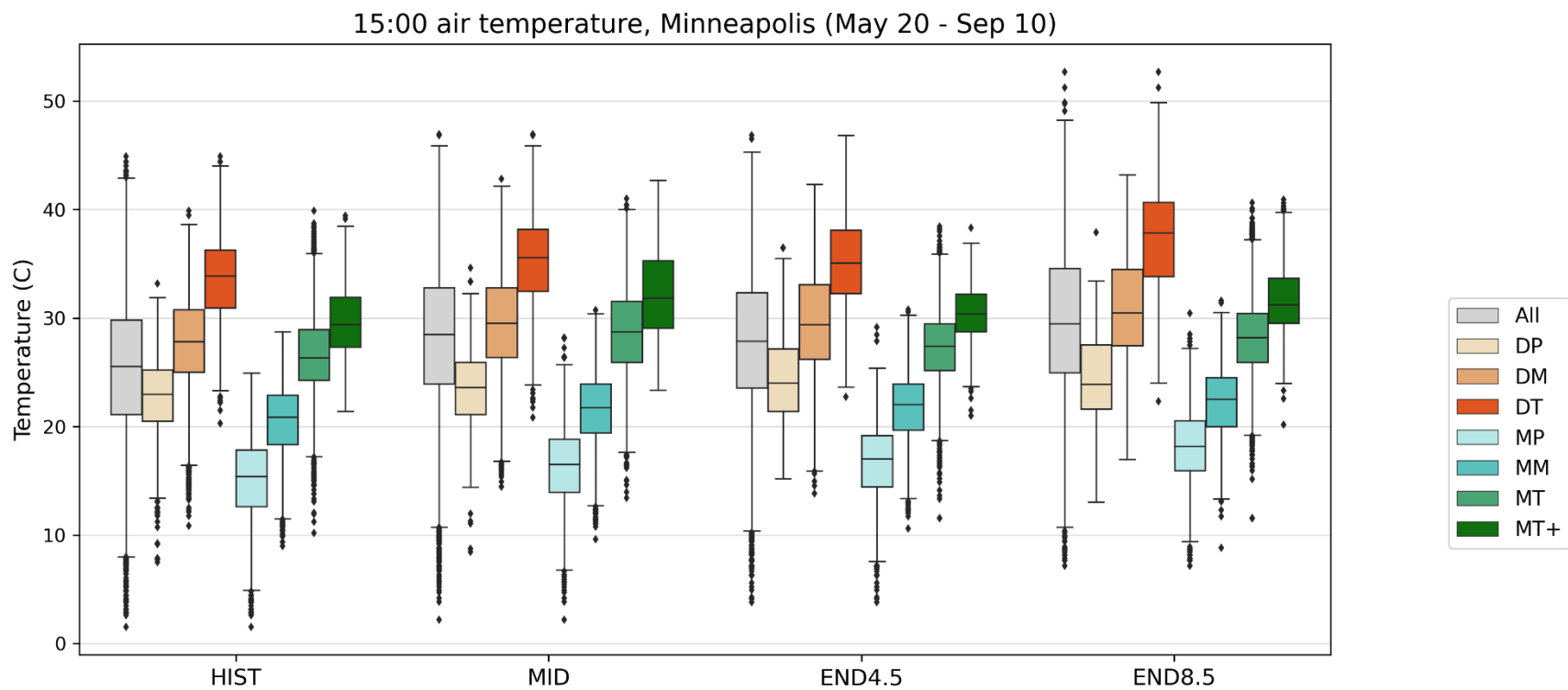


Figure 4.9: Distributions of 15:00 air temperatures by scenario, across all summer (May 20-September 10) days and within individual summer air mass types. Each observation represents one day (see Table 4.3 description).

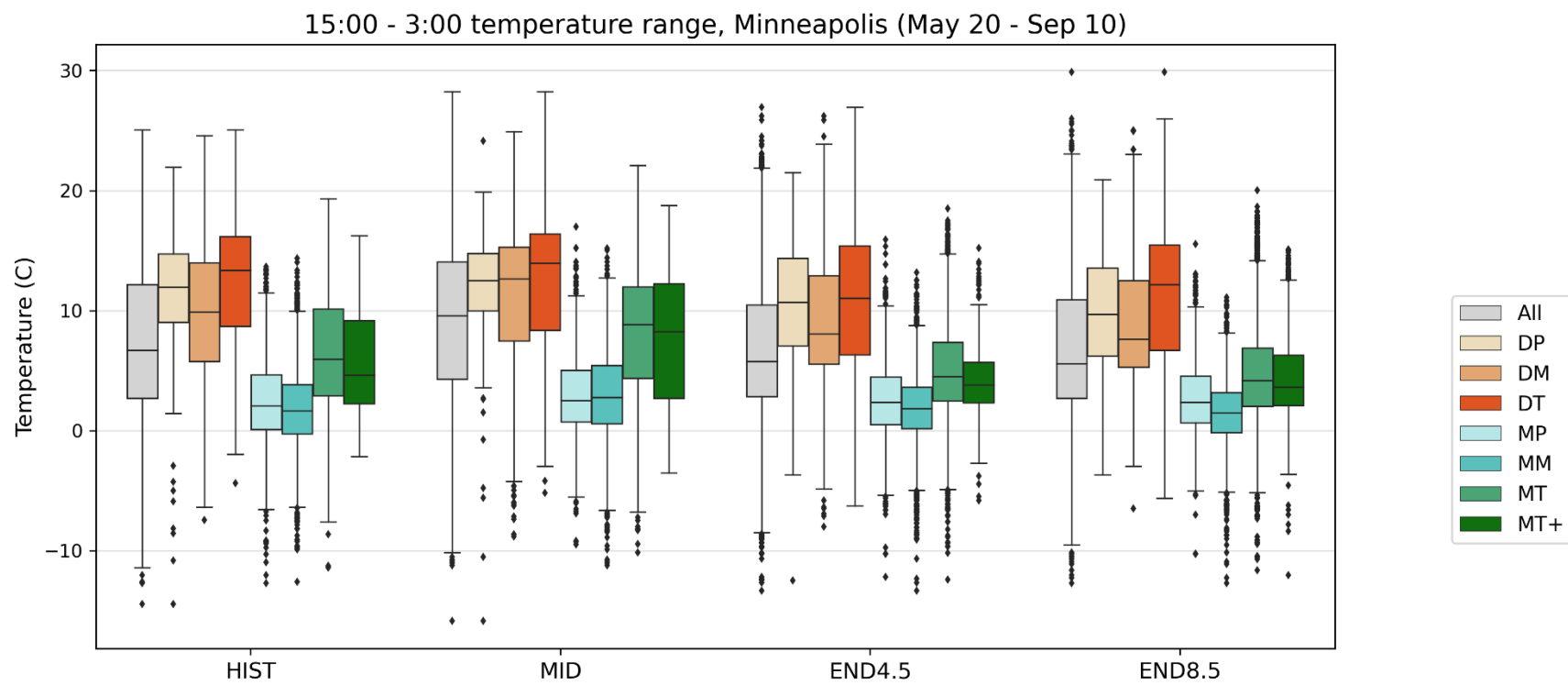


Figure 4.10: As Figure 4.9, but for diurnal air temperature ranges between 15:00 and 3:00.

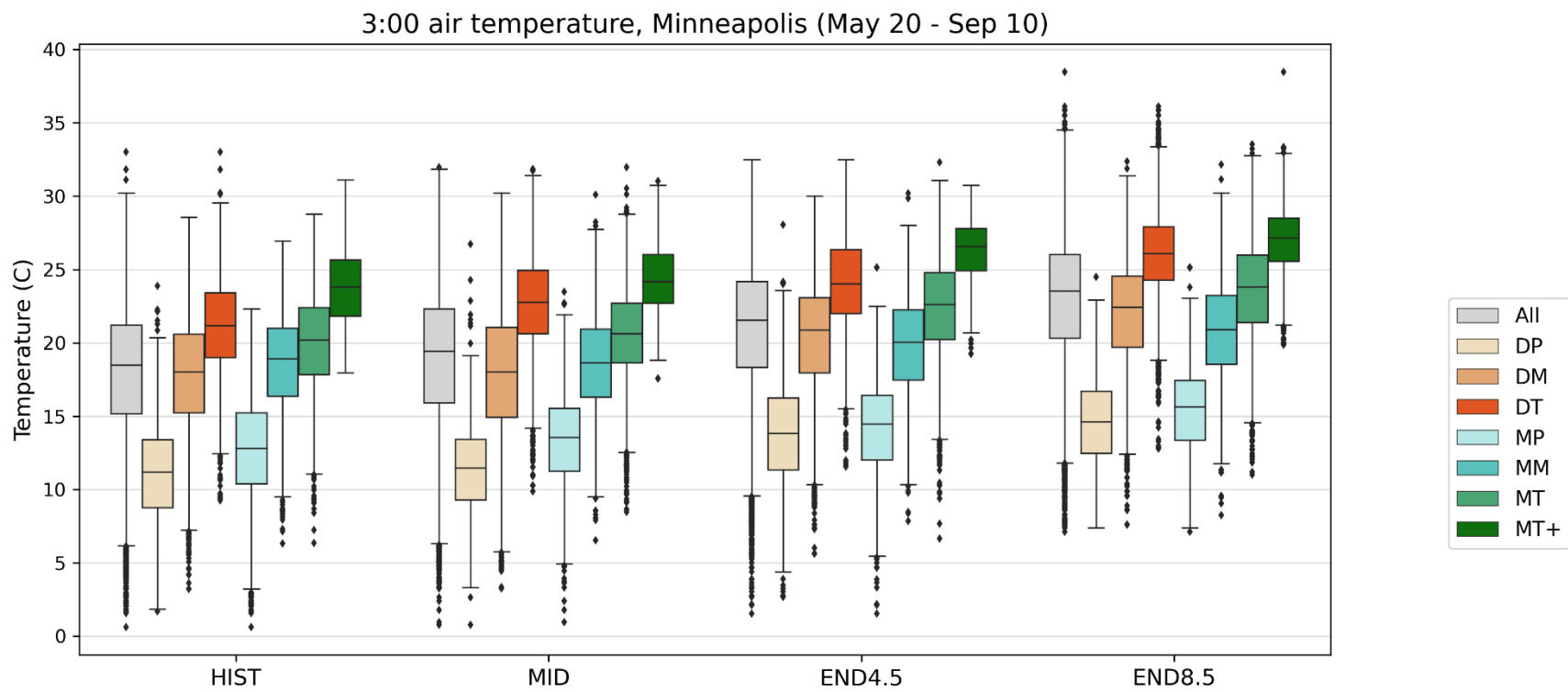


Figure 4.11: As Figure 4.9, but for 3:00 air temperatures.

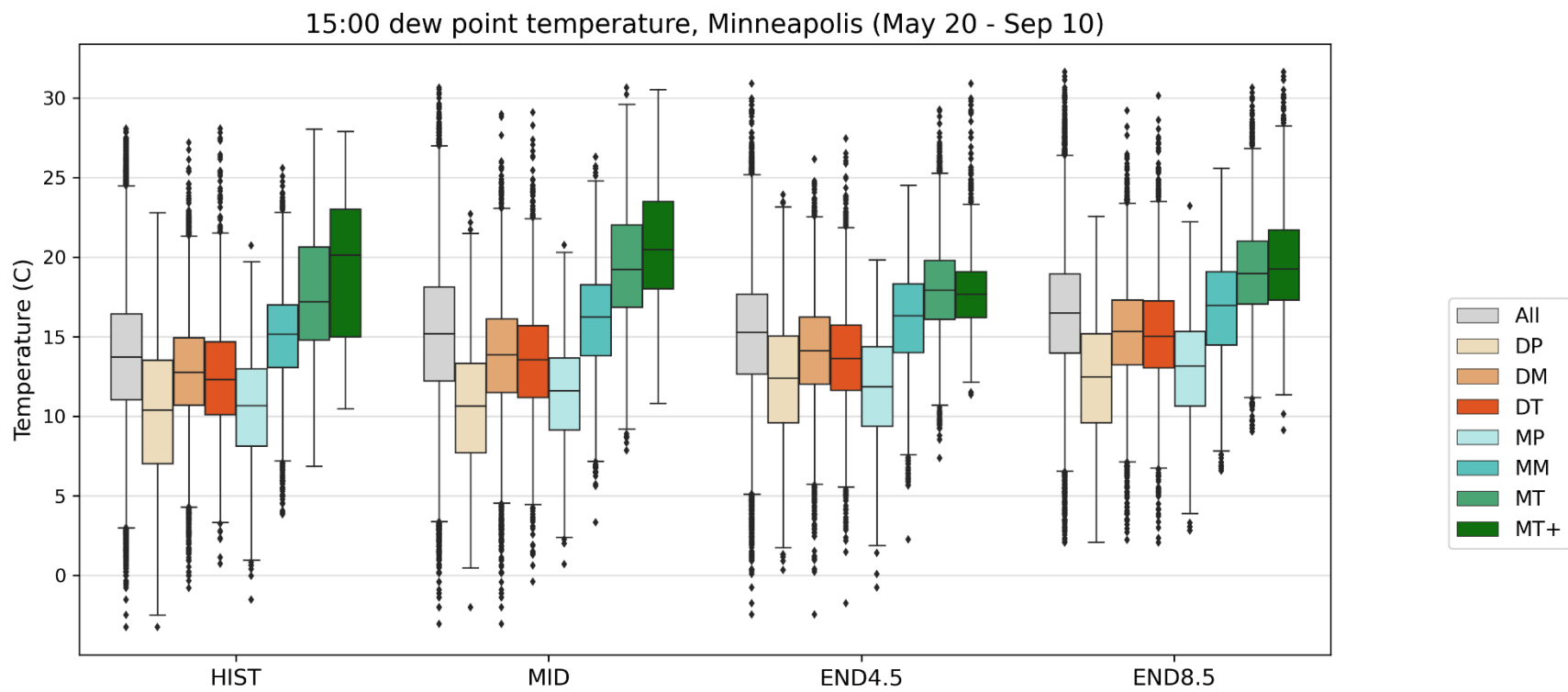


Figure 4.12: As Figure 4.9, but for 15:00 dew point temperatures.

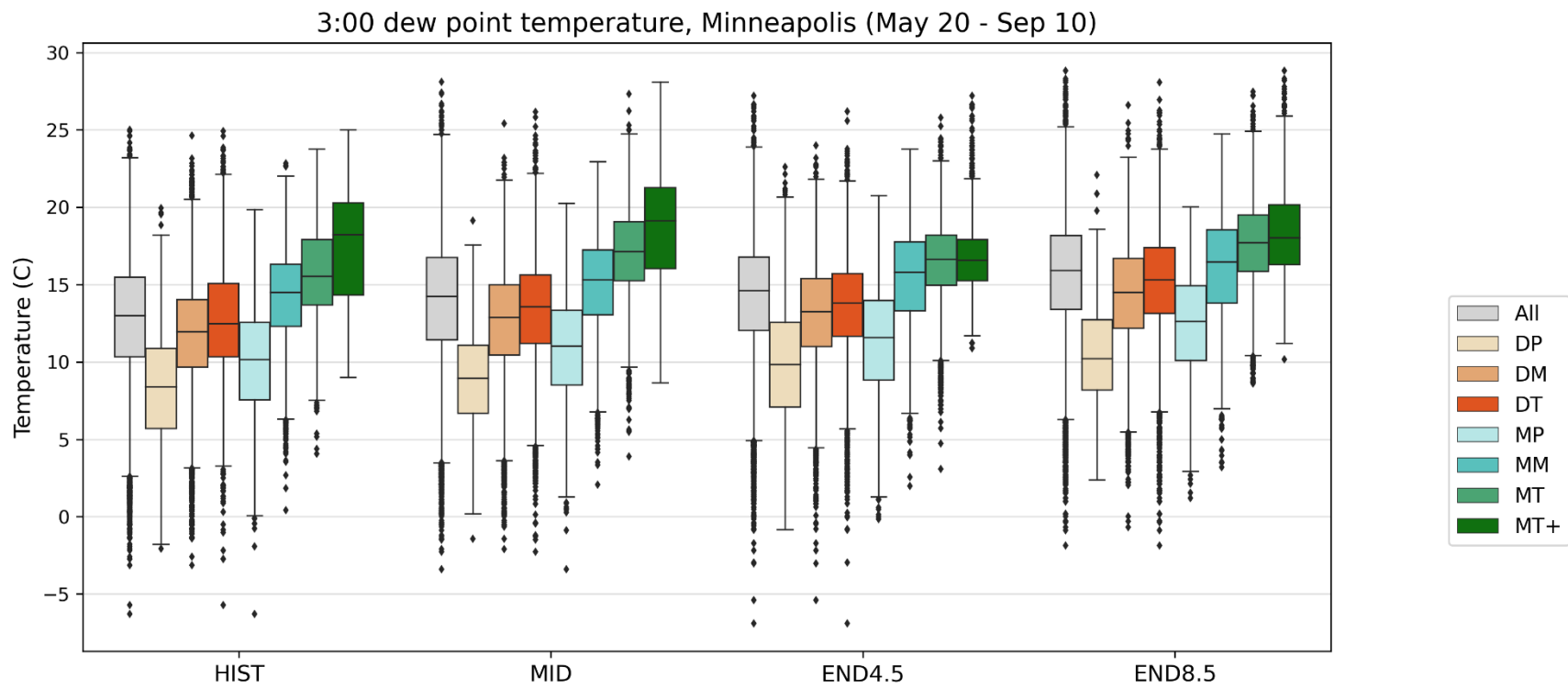


Figure 4.13: As Figure 4.9, but for 3:00 dew point temperatures.

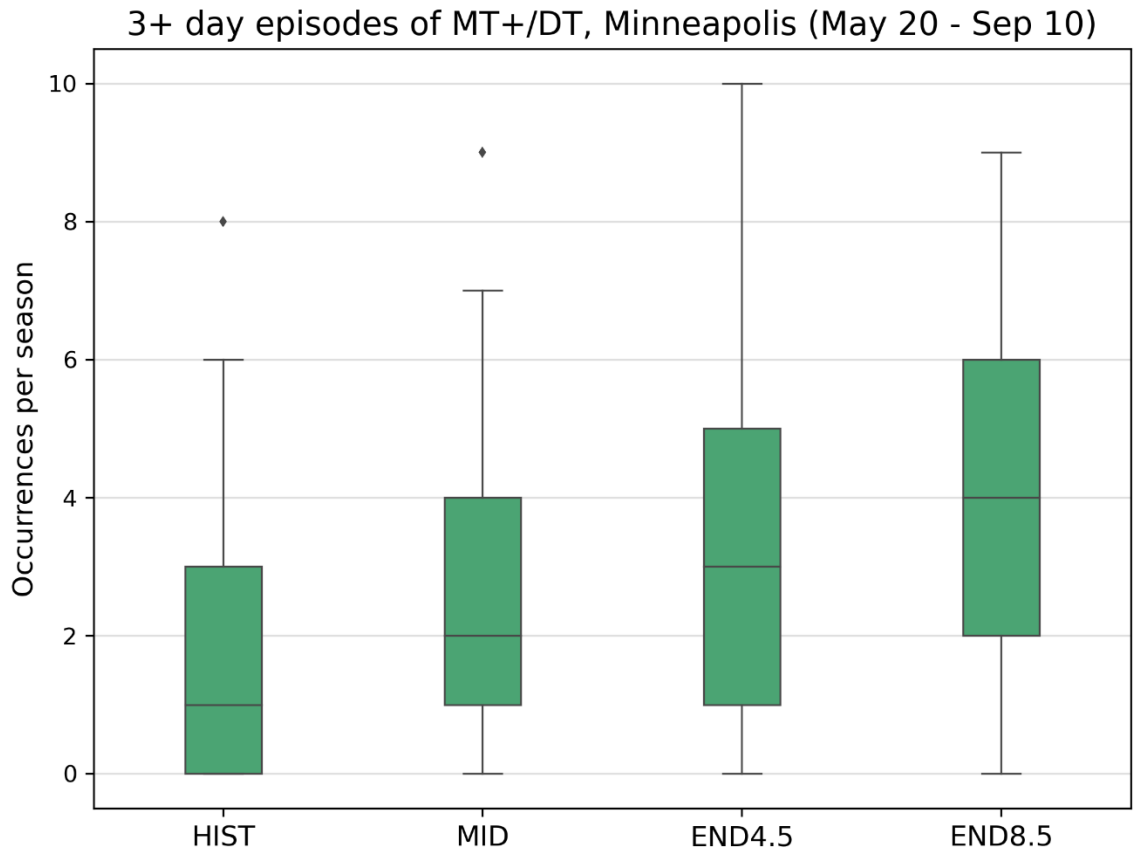


Figure 4.14: Distributions of annual episode frequency of 3 or more consecutive MT+/DT days by scenario, within the May 20-September 10 season. Each observation represents one model-year combination (see Table 4.2 description).

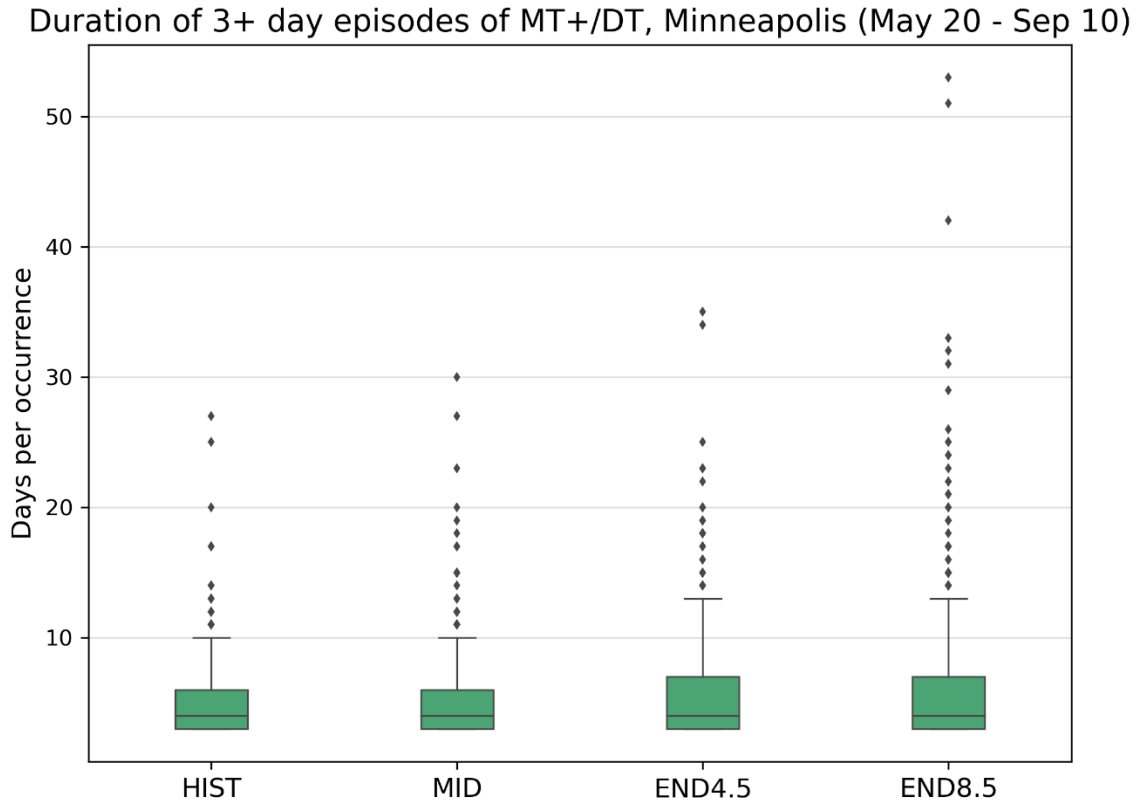


Figure 4.15: Distributions of episode durations of 3 or more consecutive MT+/DT days by scenario, within the May 20-September 10 season. Each observation represents one 3+ day episode (see Table 4.2 description).

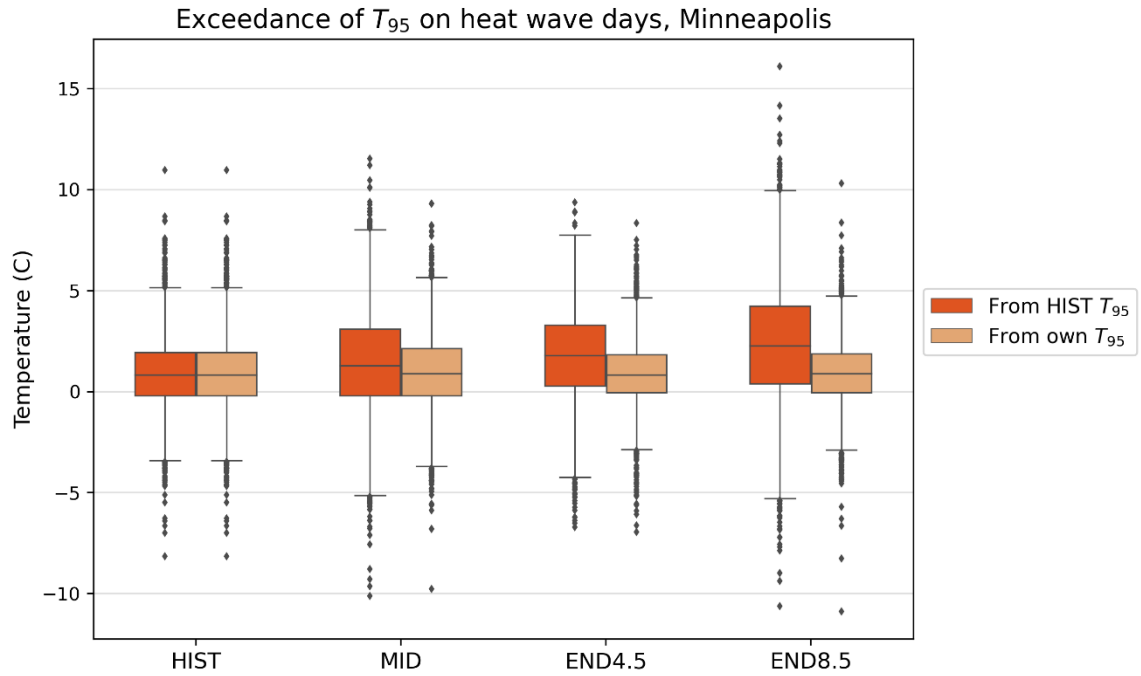


Figure 4.16: Distributions of exceedances of T_{95} on heat wave days by scenario. Each observation represents one heat wave day.

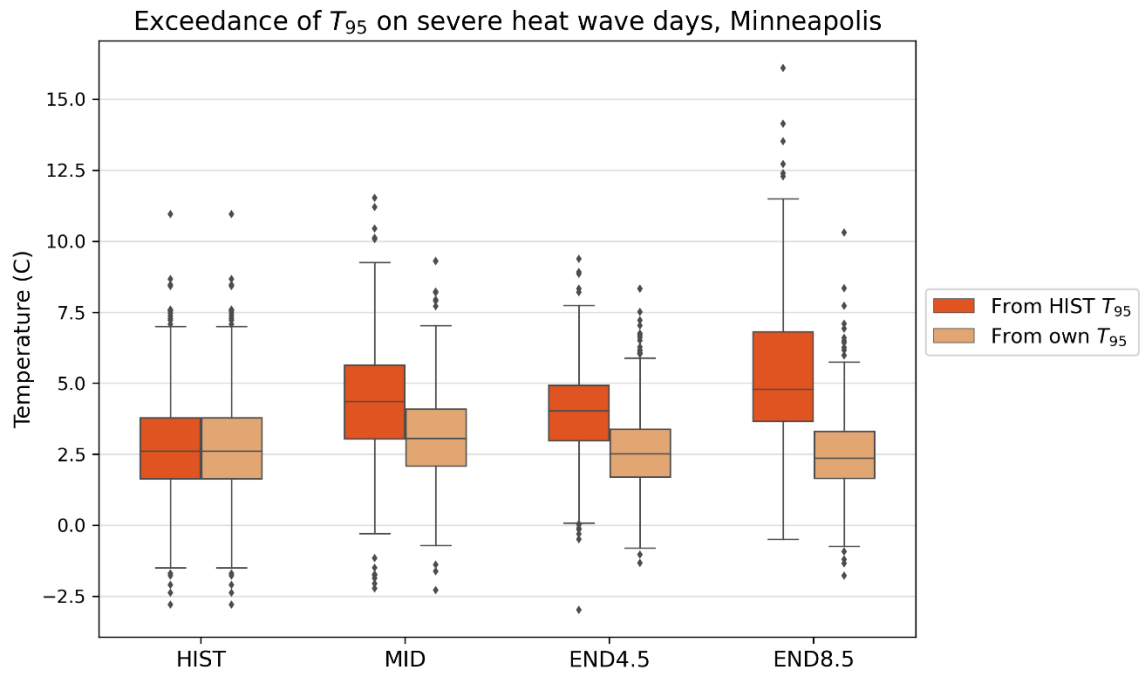


Figure 4.17: As Figure 4.16, but including only days within severe heat waves.

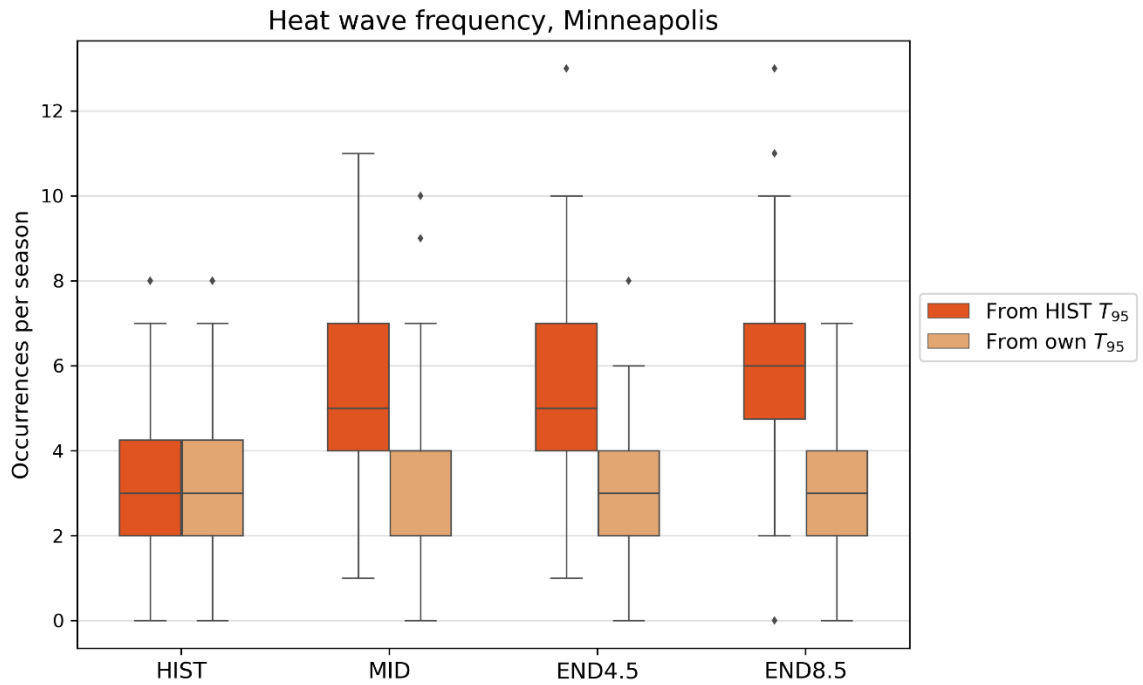


Figure 4.18: Distributions of annual frequency of positive-EHF heat wave events by scenario. Each observation represents one model-year combination (see Table 4.4 description).

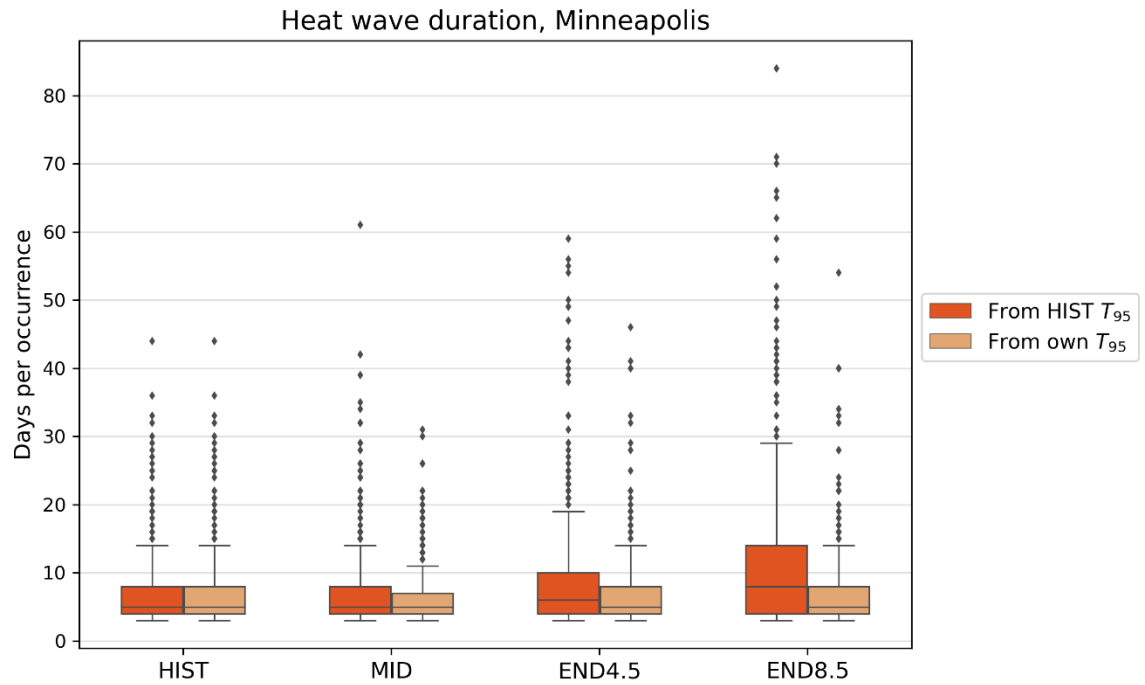


Figure 4.19: Distributions of heat wave durations by scenario. Each observation represents one heat wave event.

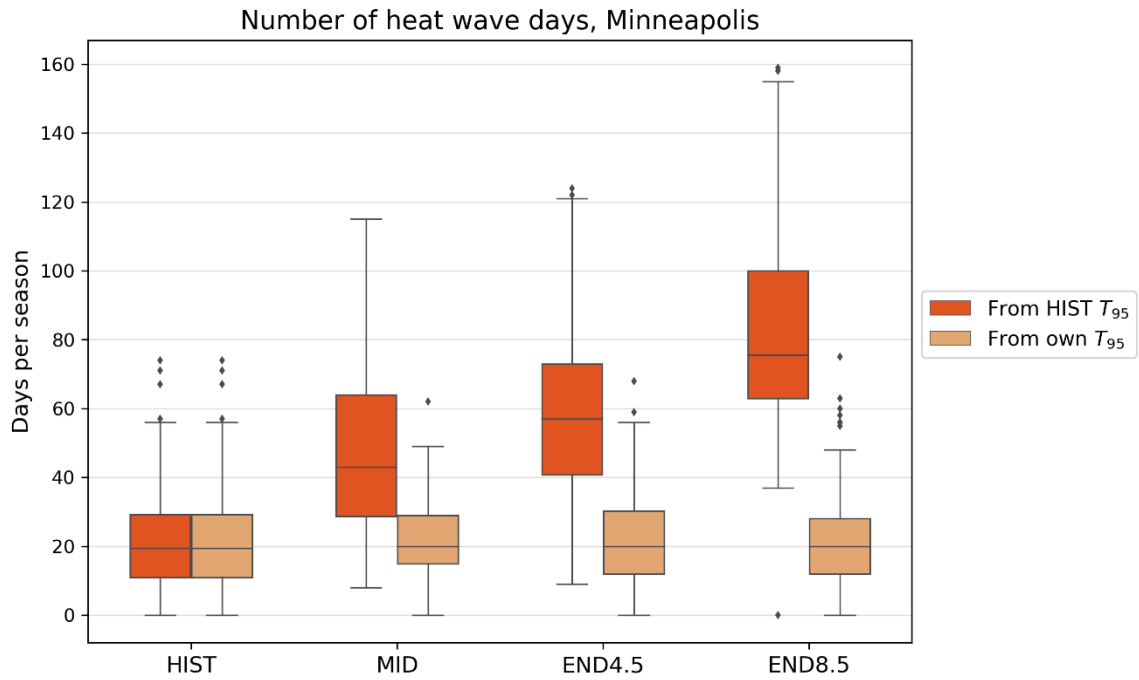


Figure 4.20: Distributions of annual frequency of individual heat wave days by scenario. Each observation represents one model-year combination.

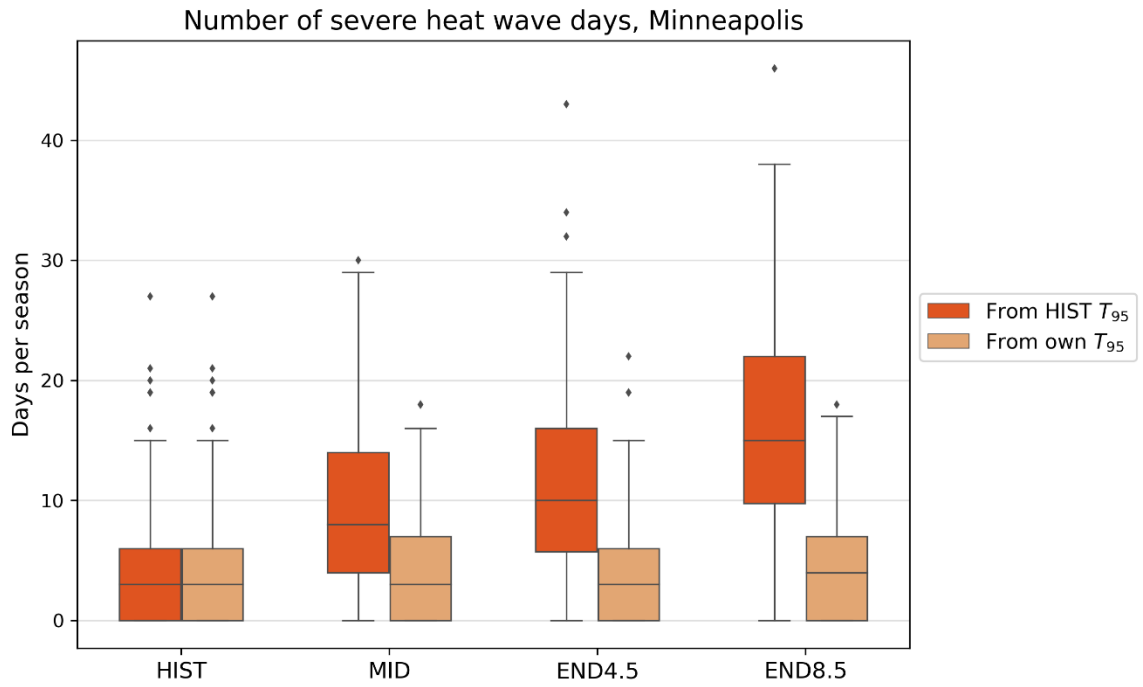


Figure 4.21: As Figure 4.20, but counting only days within severe heat waves.

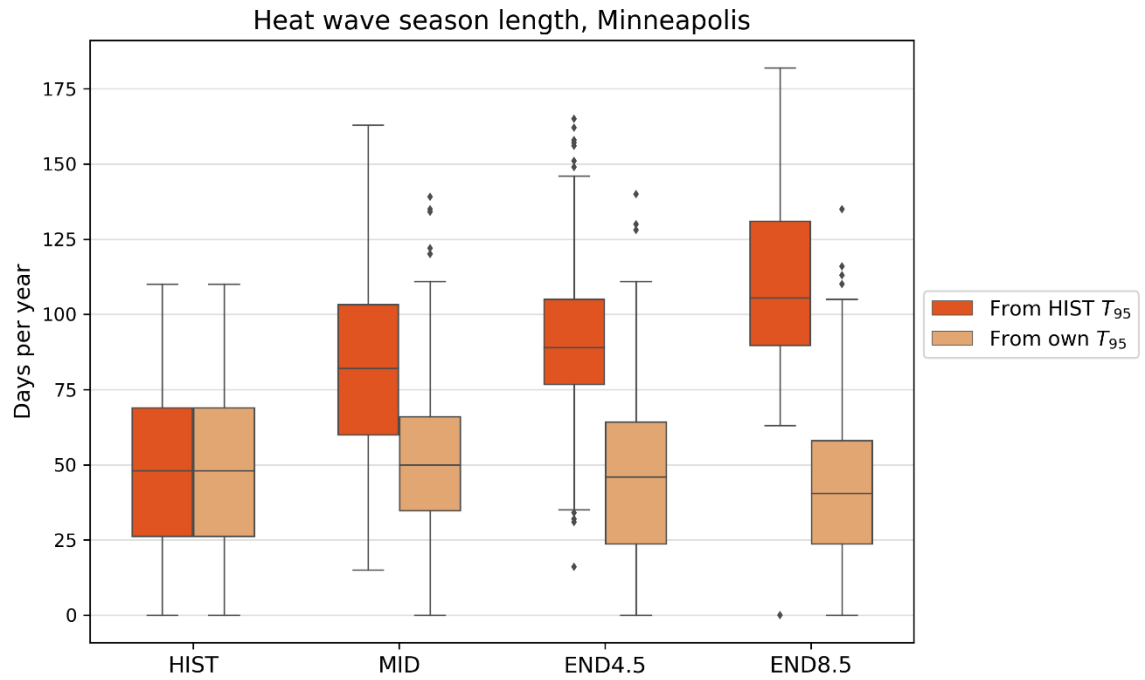


Figure 4.22: Distributions of heat wave season lengths by scenario. Each observation represents one model-year combination.

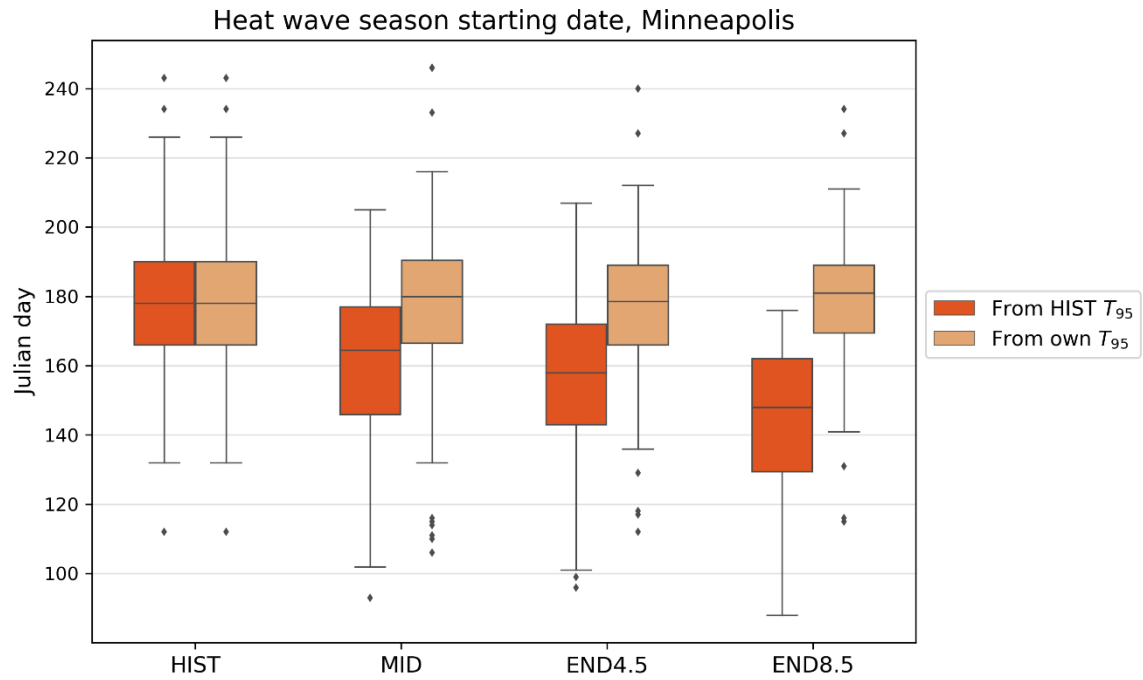


Figure 4.23: Distributions of heat wave season starting dates by scenario. Each observation represents one model-year combination.

Bibliography

- Anderson, B. G., & Bell, M. L. (2009). Weather-related mortality: How heat, cold, and heat waves affect mortality in the United States. *Epidemiology*, 20(2), 205–213. <https://doi.org/10.1097/EDE.0b013e318190ee08>
- Arbuthnott, K., Hajat, S., Heaviside, C., & Vardoulakis, S. (2016). Changes in population susceptibility to heat and cold over time: Assessing adaptation to climate change. *Environmental Health: A Global Access Science Source*, 15, S33. <https://doi.org/10.1186/s12940-016-0102-7>
- Basu, R., & Samet, J. M. (2002). Relation between Elevated Ambient Temperature and Mortality: A Review of the Epidemiologic Evidence. *Epidemiologic Reviews*, 24(2), 190–202. <https://doi.org/10.1093/EPIREV/MXF007>
- Bergeron, T. (1930). Richtlinien einer dynamischen klimatologie. *Meteorologische Zeitschrift*, 47, 246–262.
- Curriero, F. C., Heiner, K. S., Samet, J. M., Zeger, S. L., Strug, L., & Patz, J. A. (2002). Temperature and mortality in 11 cities of the eastern United States. *American Journal of Epidemiology*, 155(1), 80–87. <https://doi.org/10.1093/aje/155.1.80>
- Dahl, K., Licker, R., Abatzoglou, J. T., & Declet-Barreto, J. (2019). Increased frequency of and population exposure to extreme heat index days in the United States during the 21st century. *Environmental Research Communications*, 1(7), 075002. <https://doi.org/10.1088/2515-7620/AB27CF>
- Daly, C., Slater, M. E., Roberti, J. A., Laseter, S. H., & Swift, L. W. (2017). High-resolution precipitation mapping in a mountainous watershed: ground truth for evaluating uncertainty in a national precipitation dataset. *International Journal of Climatology*, 37, 124–137. <https://doi.org/10.1002/joc.4986>
- Davis, R. E., Knappenberger, P. C., Novicoff, W. M., & Michaels, P. J. (2002). Decadal changes in heat-related human mortality in the eastern United States. *Climate Research*, 22(2), 175–184. <https://doi.org/10.3354/CR022175>
- Dixon, P. G., Allen, M., Gosling, S. N., Hondula, D. M., Ingole, V., Lucas, R., & Vanos, J. (2016). Perspectives on the Synoptic Climate Classification and its Role in Interdisciplinary Research. *Geography Compass*, 10(4), 147–164. <https://doi.org/10.1111/gec3.12264>
- Dufresne, J. L., & Bony, S. (2008). An assessment of the primary sources of spread of

- global warming estimates from coupled atmosphere-ocean models. *Journal of Climate*, 21(19), 5135–5144. <https://doi.org/10.1175/2008JCLI2239.1>
- Dunne, J. P., John, J. G., Adcroft, A. J., Griffies, S. M., Hallberg, R. W., Shevliakova, E., et al. (2012). GFDL's ESM2 global coupled climate-carbon earth system models. Part I: Physical formulation and baseline simulation characteristics. *Journal of Climate*, 25(19), 6646–6665. <https://doi.org/10.1175/JCLI-D-11-00560.1>
- Fischer, E. M., Oleson, K. W., & Lawrence, D. M. (2012). Contrasting urban and rural heat stress responses to climate change. *Geophysical Research Letters*, 39(3). <https://doi.org/10.1029/2011GL050576>
- Founda, D., & Santamouris, M. (2017). Synergies between Urban Heat Island and Heat Waves in Athens (Greece), during an extremely hot summer (2012). *Scientific Reports*, 7(1). <https://doi.org/10.1038/s41598-017-11407-6>
- Gent, P. R., Danabasoglu, G., Donner, L. J., Holland, M. M., Hunke, E. C., Jayne, S. R., et al. (2011). The community climate system model version 4. *Journal of Climate*, 24(19), 4973–4991. <https://doi.org/10.1175/2011JCLI4083.1>
- Gronlund, C. J. (2014). Racial and Socioeconomic Disparities in Heat-Related Health Effects and Their Mechanisms: a Review. *Current Epidemiology Reports*, 1(3), 165–173. <https://doi.org/10.1007/s40471-014-0014-4>
- de Guzman, E., Kalkstein, L. S., Sailor, D., Eisenman, D., Sheridan, S., Kirner, K., et al. (2020). *Rx for Hot Cities: Climate Resilience Through Urban Greening and Cooling in Los Angeles*.
- Habeeb, D., Vargo, J., & Stone, B. (2015). Rising heat wave trends in large US cities. *Natural Hazards*, 76(3), 1651–1665. <https://doi.org/10.1007/s11069-014-1563-z>
- Hajat, S., Armstrong, B., Baccini, M., Biggeri, A., Bisanti, L., Russo, A., et al. (2006). Impact of high temperatures on mortality: Is there an added heat wave effect? *Epidemiology*, 17(6), 632–638. <https://doi.org/10.1097/01.ede.0000239688.70829.63>
- Harlan, S. L., Brazel, A. J., Prashad, L., Stefanov, W. L., & Larsen, L. (2006). Neighborhood microclimates and vulnerability to heat stress. *Social Science & Medicine*, 63, 2847–2863. <https://doi.org/10.1016/j.socscimed.2006.07.030>
- Hayhoe, K., Sheridan, S., Kalkstein, L., & Greene, S. (2010). Climate change, heat waves, and mortality projections for Chicago. *Journal of Great Lakes Research*, 36(SUPPL. 2), 65–73. <https://doi.org/10.1016/j.jglr.2009.12.009>

- Hoffman, J. S., Shandas, V., & Pendleton, N. (2020). The Effects of Historical Housing Policies on Resident Exposure to Intra-Urban Heat: A Study of 108 US Urban Areas. *Climate*, 8(1), 12. <https://doi.org/10.3390/cli8010012>
- Hondula, D. M., Vanos, J. K., & Gosling, S. N. (2014). The SSC: A decade of climate-health research and future directions. *International Journal of Biometeorology*, 58(2), 109–120. <https://doi.org/10.1007/s00484-012-0619-6>
- Kalkstein, A. J., Kalkstein, L. S., Vanos, J. K., Eisenman, D. P., & Grady Dixon, P. (2018). Heat/mortality sensitivities in Los Angeles during winter: A unique phenomenon in the United States. *Environmental Health: A Global Access Science Source*, 17(1), 45. <https://doi.org/10.1186/s12940-018-0389-7>
- Kalkstein, L. S., & Davis, R. E. (1989). Weather and Human Mortality: An Evaluation of Demographic and Interregional Responses in the United States. *Annals of the Association of American Geographers*, 79(1), 44–64. <https://doi.org/10.1111/j.1467-8306.1989.tb00249.x>
- Kalkstein, L. S., & Greene, J. S. (1997). An evaluation of climate/mortality relationships in large U.S. cities and the possible impacts of a climate change. *Environmental Health Perspectives*, 105(1), 84–93. <https://doi.org/10.1289/ehp.9710584>
- Kalkstein, L. S., Nichols, M. C., David Barthel, C., & Scott Greene, J. (1996). A new spatial synoptic classification: Application to air-mass analysis. *International Journal of Climatology*, 16(9), 983–1004. [https://doi.org/10.1002/\(SICI\)1097-0088\(199609\)16:9<983::AID-JOC61>3.0.CO;2-N](https://doi.org/10.1002/(SICI)1097-0088(199609)16:9<983::AID-JOC61>3.0.CO;2-N)
- Kalkstein, L. S., Sheridan, S. C., & Graybeal, D. Y. (1998). A determination of character and frequency changes in air masses using a spatial synoptic classification. *International Journal of Climatology*, 18(11), 1223–1236. [https://doi.org/10.1002/\(SICI\)1097-0088\(199809\)18:11<1223::AID-JOC310>3.0.CO;2-1](https://doi.org/10.1002/(SICI)1097-0088(199809)18:11<1223::AID-JOC310>3.0.CO;2-1)
- Kalkstein, L. S., Greene, S., Mills, D. M., & Samenow, J. (2011). An evaluation of the progress in reducing heat-related human mortality in major U.S. cities. *Natural Hazards*, 56(1), 113–129. <https://doi.org/10.1007/s11069-010-9552-3>
- Kinney, P. L., O'Neill, M. S., Bell, M. L., & Schwartz, J. (2008). Approaches for estimating effects of climate change on heat-related deaths: challenges and opportunities. *Environmental Science & Policy*, 11(1), 87–96. <https://doi.org/10.1016/J.ENVSCI.2007.08.001>
- Knight, D. B., Davis, R. E., Sheridan, S. C., Hondula, D. M., Sitka, L. J., Deaton, M., et

- al. (2008). Increasing frequencies of warm and humid air masses over the conterminous United States from 1948 to 2005. *Geophysical Research Letters*, 35(10). <https://doi.org/10.1029/2008GL033697>
- Lau, N. C., & Nath, M. J. (2012). A model study of heat waves over North America: Meteorological aspects and projections for the twenty-first century. *Journal of Climate*, 25(14), 4761–4764. <https://doi.org/10.1175/JCLI-D-11-00575.1>
- Lee, W. V. (2013). Historical global analysis of occurrences and human casualty of extreme temperature events (ETEs). *Natural Hazards* 2013 70:2, 70(2), 1453–1505. <https://doi.org/10.1007/S11069-013-0884-7>
- Li, B., Sain, S., Mearns, L. O., Anderson, H. A., Kovats, S., Ebi, K. L., et al. (2012). The impact of extreme heat on morbidity in Milwaukee, Wisconsin. *Climatic Change*, 110(3–4), 959–976. <https://doi.org/10.1007/s10584-011-0120-y>
- Liess, S., Twine, T. E., Snyder, P. K., Hutchison, W. D., Konar-Steenberg, G., Keeler, B. L., & Brauman, K. A. (2021). High-resolution Climate Projections over Minnesota for the 21st Century. *JGR-Atmospheres*, (Preprint), 26. <https://doi.org/10.1002/ESSOAR.10507340.2>
- Loridan, T., Coates, L., Frontiers, R., Argüeso, D., & Perkins-Kirkpatrick, S. E. (2016). *The excess heat factor as a metric for heat-related fatalities: Defining heatwave risk categories. Australian Journal of Emergency Management* (Vol. 31).
- Luber, G., & McGeehin, M. (2008, November 1). Climate Change and Extreme Heat Events. *American Journal of Preventive Medicine*. Elsevier. <https://doi.org/10.1016/j.amepre.2008.08.021>
- Lyon, B., & Dole, R. M. (1995). A diagnostic comparison of the 1980 and 1988 US summer heat wave- droughts. *Journal of Climate*, 8(6), 1658–1675. [https://doi.org/10.1175/1520-0442\(1995\)008<1658:ADCOTA>2.0.CO;2](https://doi.org/10.1175/1520-0442(1995)008<1658:ADCOTA>2.0.CO;2)
- Meehl, G. A., & Tebaldi, C. (2004). More intense, more frequent, and longer lasting heat waves in the 21st century. *Science*, 305(5686), 994–997. <https://doi.org/10.1126/science.1098704>
- Minnesota Department of Natural Resources. (1989). *Drought of 1988*. St. Paul, Minn.: Minnesota Dept. of Natural Resources, Division of Waters.
- Nairn, J. R., & Fawcett, R. J. B. (2014). The excess heat factor: A metric for heatwave intensity and its use in classifying heatwave severity. *International Journal of Environmental Research and Public Health*, 12(1), 227–253.

<https://doi.org/10.3390/ijerph120100227>

- Nairn, J. R., Ostendorf, B., & Bi, P. (2018). Performance of excess heat factor severity as a global heatwave health impact index. *International Journal of Environmental Research and Public Health*, 15(11). <https://doi.org/10.3390/ijerph15112494>
- Noe, R. R., Keeler, B. L., Twine, T. E., Brauman, K. A., Mayer, T., & Rogers, M. (2019). *Climate change projections for improved management of infrastructure, industry, and water resources in Minnesota*.
- Pincus, R., Batstone, C. P., Patrick Hofmann, R. J., Taylor, K. E., & Glecker, P. J. (2008). Evaluating the present-day simulation of clouds, precipitation, and radiation in climate models. *Journal of Geophysical Research Atmospheres*, 113(14), D14209. <https://doi.org/10.1029/2007JD009334>
- Scalley, B. D., Spicer, T., Jian, L., Xiao, J., Nairn, J., Robertson, A., & Weeramanthri, T. (2015). Responding to heatwave intensity: Excess Heat Factor is a superior predictor of health service utilisation and a trigger for heatwave plans. *Australian and New Zealand Journal of Public Health*, 39(6), 582–587. <https://doi.org/10.1111/1753-6405.12421>
- Scoccimarro, E., Gualdi, S., Bellucci, A., Sanna, A., Fogli, P. G., Manzini, E., et al. (2011). Effects of tropical cyclones on ocean heat transport in a high-resolution coupled general circulation model. *Journal of Climate*, 24(16), 4368–4384. <https://doi.org/10.1175/2011JCLI4104.1>
- Semenza, J. C., McCullough, J. E., Flanders, W. D., McGeehin, M. A., & Lumpkin, J. R. (1999). Excess hospital admissions during the July 1995 heat wave in Chicago. *American Journal of Preventive Medicine*, 16(4), 269–277. [https://doi.org/10.1016/S0749-3797\(99\)00025-2](https://doi.org/10.1016/S0749-3797(99)00025-2)
- Sheridan, S. C. (2002). The redevelopment of a weather-type classification scheme for North America. *International Journal of Climatology*, 22(1), 51–68. <https://doi.org/10.1002/joc.709>
- Sheridan, S. C., & Dixon, P. G. (2017). Spatiotemporal trends in human vulnerability and adaptation to heat across the United States. *Anthropocene*, 20, 61–73. <https://doi.org/10.1016/j.ancene.2016.10.001>
- Sheridan, S. C., & Kalkstein, A. J. (2010). Seasonal variability in heat-related mortality across the United States. *Natural Hazards*, 55(2), 291–305. <https://doi.org/10.1007/s11069-010-9526-5>

- Sheridan, S. C., & Kalkstein, L. S. (2004). Progress in heat watch-warning system technology. *Bulletin of the American Meteorological Society*, 85(12), 1931–1941. <https://doi.org/10.1175/BAMS-85-12-1931>
- Sheridan, S. C., Kalkstein, L. S., & Scott, J. M. (2000). An evaluation of the variability of Air mass character between urban and rural areas. In: *Biometeorology and Urban Climatology at the Turn of the Millennium*, (1), 487–490.
- Sheridan, S. C., Kalkstein, A. J., & Kalkstein, L. S. (2009). Trends in heat-related mortality in the United States, 1975-2004. *Natural Hazards*, 50(1), 145–160. <https://doi.org/10.1007/s11069-008-9327-2>
- Sheridan, S. C., Allen, M. J., Lee, C. C., & Kalkstein, L. S. (2012). Future heat vulnerability in California, Part II: Projecting future heat-related mortality. *Climatic Change*, 115(2), 311–326. <https://doi.org/10.1007/s10584-012-0437-1>
- Sheridan, S. C., Grady Dixon, P., Kalkstein, A. J., & Allen, M. J. (2021). Recent trends in heat-related mortality in the united states: An update through 2018. *Weather, Climate, and Society*, 13(1), 95–106. <https://doi.org/10.1175/WCAS-D-20-0083.1>
- Smoliak, B. V., Snyder, P. K., Twine, T. E., Mykleby, P. M., & Hertel, W. F. (2015). Dense network observations of the Twin Cities Canopy-Layer urban heat island. *Journal of Applied Meteorology and Climatology*, 54(9), 1899–1917. <https://doi.org/10.1175/JAMC-D-14-0239.1>
- Steadman, R. G. (1994). Norms of apparent temperature in Australia. *Australian Meteorological Magazine*, 43(1), 1–16.
- Teutschbein, C., & Seibert, J. (2012). Bias correction of regional climate model simulations for hydrological climate-change impact studies: Review and evaluation of different methods. *Journal of Hydrology*, 456–457, 12–29. <https://doi.org/10.1016/j.jhydrol.2012.05.052>
- United States Environmental Protection Agency Office of Atmospheric Programs. (2006). Excessive Heat Events Guidebook. *Environmental Protection*, (June), 60pp.
- Vanos, J. K., Kalkstein, L. S., & Sanford, T. J. (2015). Detecting synoptic warming trends across the US Midwest and implications to human health and heat-related mortality. *International Journal of Climatology*, 35(1), 85–96. <https://doi.org/10.1002/joc.3964>
- Vicedo-Cabrera, A. M., Scovronick, N., Sera, F., Royé, D., Schneider, R., Tobias, A., et al. (2021). The burden of heat-related mortality attributable to recent human-induced

- climate change. *Nature Climate Change*, 11(6), 492–500.
<https://doi.org/10.1038/s41558-021-01058-x>
- Voldoire, A., Sanchez-Gomez, E., Salas y Mélia, D., Decharme, B., Cassou, C., Sénési, S., et al. (2013). The CNRM-CM5.1 global climate model: Description and basic evaluation. *Climate Dynamics*, 40(9–10), 2091–2121.
<https://doi.org/10.1007/s00382-011-1259-y>
- Watanabe, M., Suzuki, T., O’Ishi, R., Komuro, Y., Watanabe, S., Emori, S., et al. (2010). Improved climate simulation by MIROC5: Mean states, variability, and climate sensitivity. *Journal of Climate*, 23(23), 6312–6335.
<https://doi.org/10.1175/2010JCLI3679.1>
- Watts, J. D., & Kalkstein, L. S. (2004). The development of a warm-weather relative stress index for environmental applications. *Journal of Applied Meteorology*, 43(3), 503–513. [https://doi.org/10.1175/1520-0450\(2004\)043<0503:TDOAWR>2.0.CO;2](https://doi.org/10.1175/1520-0450(2004)043<0503:TDOAWR>2.0.CO;2)
- Wilson, B. (2020). Urban Heat Management and the Legacy of Redlining. *Journal of the American Planning Association*, 86(4), 443–457.
<https://doi.org/10.1080/01944363.2020.1759127>
- Wu, T., Yu, R., Zhang, F., Wang, Z., Dong, M., Wang, L., et al. (2010). The Beijing Climate Center atmospheric general circulation model: Description and its performance for the present-day climate. *Climate Dynamics*, 34(1), 123–147.
<https://doi.org/10.1007/s00382-008-0487-2>
- Yukimoto, S., Adachi, Y., Hosaka, M., Sakami, T., Yoshimura, H., Hirabara, M., et al. (2012). A new global climate model of the Meteorological Research Institute: MRI-CGCM3: -Model description and basic performance-. *Journal of the Meteorological Society of Japan*, 90(A), 23–64. <https://doi.org/10.2151/jmsj.2012-A02>

ProQuest Number: 28774811

INFORMATION TO ALL USERS

The quality and completeness of this reproduction is dependent on the quality and completeness of the copy made available to ProQuest.



Distributed by ProQuest LLC (2021).

Copyright of the Dissertation is held by the Author unless otherwise noted.

This work may be used in accordance with the terms of the Creative Commons license or other rights statement, as indicated in the copyright statement or in the metadata associated with this work. Unless otherwise specified in the copyright statement or the metadata, all rights are reserved by the copyright holder.

This work is protected against unauthorized copying under Title 17,
United States Code and other applicable copyright laws.

Microform Edition where available © ProQuest LLC. No reproduction or digitization of the Microform Edition is authorized without permission of ProQuest LLC.

ProQuest LLC
789 East Eisenhower Parkway
P.O. Box 1346
Ann Arbor, MI 48106 - 1346 USA